

1 SEARCH FOR PRODUCTION OF A HIGGS BOSON AND A SINGLE TOP  
2 QUARK IN MULTILEPTON FINAL STATES IN  $pp$  COLLISIONS AT  $\sqrt{s} = 13$   
3 TeV.

4 by

5 Jose Andres Monroy Montañez

6 A DISSERTATION

7 Presented to the Faculty of

8 The Graduate College at the University of Nebraska

In Partial Fulfilment of Requirements

10 For the Degree of Doctor of Philosophy

11 Major: Physics and Astronomy

12 Under the Supervision of Kenneth Bloom and Aaron Dominguez

13 Lincoln, Nebraska

14 July, 2018

15 SEARCH FOR PRODUCTION OF A HIGGS BOSON AND A SINGLE TOP  
16 QUARK IN MULTILEPTON FINAL STATES IN pp COLLISIONS AT  $\sqrt{s} = 13$   
17 TeV.

18 Jose Andres Monroy Montañez, Ph.D.  
19 University of Nebraska, 2018

20 Adviser: Kenneth Bloom and Aaron Dominguez

# <sup>21</sup> Table of Contents

<sup>22</sup>	<b>Table of Contents</b>	<b>iii</b>
<sup>23</sup>	<b>List of Figures</b>	<b>v</b>
<sup>24</sup>	<b>List of Tables</b>	<b>vii</b>
<sup>25</sup>	<b>1 INTRODUCTION</b>	<b>1</b>
<sup>26</sup>	<b>2 Theoretical approach</b>	<b>2</b>
<sup>27</sup>	2.1 Introduction . . . . .	2
<sup>28</sup>	2.2 Standard model of particle physics . . . . .	3
<sup>29</sup>	2.2.1 Fermions . . . . .	5
<sup>30</sup>	2.2.1.1 Leptons . . . . .	6
<sup>31</sup>	2.2.1.2 Quarks . . . . .	8
<sup>32</sup>	2.2.2 Fundamental interactions . . . . .	12
<sup>33</sup>	2.2.3 Gauge bosons . . . . .	18
<sup>34</sup>	2.3 Electroweak unification and the Higgs mechanism . . . . .	20
<sup>35</sup>	2.3.1 Spontaneous symmetry breaking (SSB) . . . . .	28
<sup>36</sup>	2.3.2 Higgs mechanism . . . . .	32
<sup>37</sup>	2.3.3 Masses of the gauge bosons . . . . .	34

38	2.3.4	Masses of the fermions . . . . .	35
39	2.3.5	The Higgs field . . . . .	36
40	2.3.6	Production of Higgs bosons at LHC . . . . .	37
41	2.3.7	Higgs boson decay channels . . . . .	41
42	2.4	Associated production of a Higgs boson and a single Top quark. . . . .	42
43	2.5	The CP-mixing in tH processes . . . . .	47
44	2.6	Experimantal status of the anomalous Higg-fermion coupling. . . . .	51
45	<b>3</b>	<b>The CMS experiment at the LHC</b>	<b>53</b>
46	3.1	Introduction . . . . .	53
47	3.2	The LHC . . . . .	54
48	3.3	The CMS experiment . . . . .	63
49	3.3.1	Coordinate system . . . . .	65
50	3.3.2	Pixels detector . . . . .	67
51	3.3.3	Silicon strip tracker . . . . .	69
52	3.3.4	Electromagnetic calorimeter . . . . .	70
53	3.3.5	Hadronic calorimeter . . . . .	72
54	3.3.6	Superconducting solenoid magnet . . . . .	73
55	3.3.7	Muon system . . . . .	75
56	3.3.8	CMS trigger system . . . . .	76
57	3.3.9	CMS computing . . . . .	78
58	<b>4</b>	<b>Event generation, simulation and reconstruction</b>	<b>83</b>
59	4.1	Introduction . . . . .	83
60	4.2	event generation . . . . .	83
61	4.3	Hard scattering . . . . .	83
62	4.4	parton shower . . . . .	83

63	4.5 hadronization and decays . . . . .	83
64	4.6 underlying events and pileup . . . . .	83
65	4.7 MC - MadEvent, MadGraph and madgraphNLO, powheg, pythia, tauola	83
66	4.8 detector simulation . . . . .	83
67	4.9 event reconstruction- particle flow algorithm, vertexing , muon reco,	
68	electron reco, photon and hadron reco, jets reco, anti-kt algoritm, jet	
69	energy corrections, btagging, MET . . . . .	83
70	4.10 MVA methods, NN, BDT, boosting, overtraining, variable ranking .	83
71	4.11 statistical inference, likelihood parametrization . . . . .	83
72	4.12 nuisance paraeters . . . . .	83
73	4.13 exclusion limits . . . . .	83
74	4.14 asymptotic limits . . . . .	83
75	<b>Bibliography</b>	<b>83</b>
76	<b>References</b>	<b>84</b>

## <sup>77</sup> List of Figures

78	2.1	Standard model of particle physics.	4
79	2.2	Transformations between quarks	12
80	2.3	Fundamental interactions in nature.	13
81	2.4	SM interactions diagrams	14
82	2.5	Neutral current processes	21
83	2.6	Spontaneous symmetry breaking mechanism	28
84	2.7	SSB Potential form	29
85	2.8	Potential for complex scalar field	30
86	2.9	SSB mechanism for complex scalar field	31
87	2.10	Proton-Proton collision	38
88	2.11	Higgs boson production mechanism Feynman diagrams	39
89	2.12	Higgs boson production cross section and decay branching ratios	40
90	2.13	Associated Higgs boson production mechanism Feynman diagrams	43
91	2.14	Cross section for tHq process as a function of $\kappa_t$	45
92	2.15	Cross section for $tHW$ process as a function of $\kappa_{Htt}$	46
93	2.16	NLO cross section for $tX_0$ and $t\bar{t}X_0$ .	49
94	2.17	NLO cross section for $tWX_0$ , $t\bar{t}X_0$ .	50

95	2.18 Two dimentional $\kappa_t$ - $\kappa_V$ plot of the coupling modifiers. ATLAS and CMS 96 combination. . . . .	51
97	3.1 CERN accelerator complex . . . . .	54
98	3.2 LHC protons source. First acceleration stage. . . . .	55
99	3.3 The LINAC2 accelerating system at CERN. . . . .	56
100	3.4 LHC layout and RF cavities module. . . . .	57
101	3.5 LHC dipole magnet. . . . .	59
102	3.6 Integrated luminosity delivered by LHC and recorded by CMS during 2016	61
103	3.7 LHC interaction points . . . . .	62
104	3.8 Multiple pp collision bunch crossing at CMS. . . . .	64
105	3.9 Layout of the CMS detector . . . . .	65
106	3.10 CMS detector coordinate system . . . . .	66
107	3.11 CMS pixel detector schematic view. . . . .	68
108	3.12 SST Schematic view. . . . .	69
109	3.13 CMS ECAL schematic view . . . . .	71
110	3.14 CMS HCAL schematic view . . . . .	72
111	3.15 CMS solenoid magnet . . . . .	74
112	3.16 CMS Muon system schematic view . . . . .	75
113	3.17 CMS Level-1 trigger architecture . . . . .	77
114	3.18 WLCG structure . . . . .	78
115	3.19 Data flow from CMS detector through hardware Tiers . . . . .	81

# <sup>116</sup> List of Tables

117	2.1	Fermions of the SM. . . . .	5
118	2.2	Fermion masses. . . . .	6
119	2.3	Leptons properties. . . . .	9
120	2.4	Quarks properties. . . . .	9
121	2.5	Fermion weak isospin and weak hypercharge multiplets. . . . .	11
122	2.6	Fundamental interactions features. . . . .	15
123	2.7	SM gauge bosons. . . . .	19
124	2.8	Higgs boson properties. . . . .	37
125	2.9	Predicted branching ratios for a SM Higgs boson with $m_H = 125 \text{ GeV}/c^2$ . . . . .	42
126	2.10	Predicted SM cross sections for $tH$ production at $\sqrt{s} = 13 \text{ TeV}$ . . . . .	44
127	2.11	Predicted enhancement of the $tHq$ and $tHW$ cross sections at LHC . . . . .	47

<sup>128</sup> Chapter 1

<sup>129</sup> INTRODUCTION

# <sup>130</sup> Chapter 2

## <sup>131</sup> Theoretical approach

### <sup>132</sup> 2.1 Introduction

<sup>133</sup> The physical description of the universe is a challenge that physicists have faced by  
<sup>134</sup> making theories that refine existing principles and proposing new ones in an attempt  
<sup>135</sup> to embrace emerging facts and phenomena.

<sup>136</sup>

<sup>137</sup> At the end of 1940s Julian Schwinger [1] and Richard P. Feynman [2], based in the  
<sup>138</sup> work of Sin-Itiro Tomonaga [3], developed an electromagnetic theory consistent with  
<sup>139</sup> special relativity and quantum mechanics that describes how matter and light inter-  
<sup>140</sup> act; the so-called “quantum eletrodynamics” (QED) had born.

<sup>141</sup>

<sup>142</sup> QED has become the guide in the development of theories that describe the universe.  
<sup>143</sup> It was the first example of a quantum field theory (QFT), which is the theoretical  
<sup>144</sup> framework for building quantum mechanical models that describes particles and their  
<sup>145</sup> interactions. QFT is composed of a set of mathematical tools that combines classical  
<sup>146</sup> fields, special relativity and quantum mechanics, while keeping the quantum point

147 particles and locality ideas.

148 This chapter gives an overview of the standard model of particle physics, starting  
 149 with a description of the particles and interactions that compose it, followed by a  
 150 description of the electroweak interaction, the Higgs boson and the associated pro-  
 151 duction of Higgs boson and a single top quark ( $tH$ ). The description contained in  
 152 this chapter is based on references [4–6].

## 153 2.2 Standard model of particle physics

154 Particle physics at the fundamental level is modeled in terms of a collection of in-  
 155 teracting particles and fields in a theory known as the “standard model of particle  
 156 physics (SM)”<sup>1</sup>.

157

158 The full picture of the SM is composed of three fields<sup>2</sup>, whose excitations are inter-  
 159 preted as particles called mediators or force-carriers; a set of fields, whose excitations  
 160 are interpreted as elementary particles, interacting through the exchange of those  
 161 mediators and a field that gives the mass to elementary particles. Figure 2.1 shows  
 162 an scheme of the SM particles organization. In addition to the particles in the scheme  
 163 (but not listed in it), their corresponding anti-particles, with opposite quantum num-  
 164 bers, are also part of the picture; some particles are their own anti-particles, like  
 165 photon or Higgs, or anti-particle is already listed like in the  $W^+$  and  $W^-$  case.

166

167 The mathematical formulation of the SM is based on group theory and the use of  
 168 Noether’s theorem [8] which states that for a physical system modeled by a Lagrangian

---

<sup>1</sup> The formal and complete treatment of the SM is out of the scope of this document, however a plenty of textbooks describing it at several levels are available in the literature. The treatment in references [?] is quite comprehensive and detailed.

<sup>2</sup> Note that gravitational field is not included in the standard model formulation

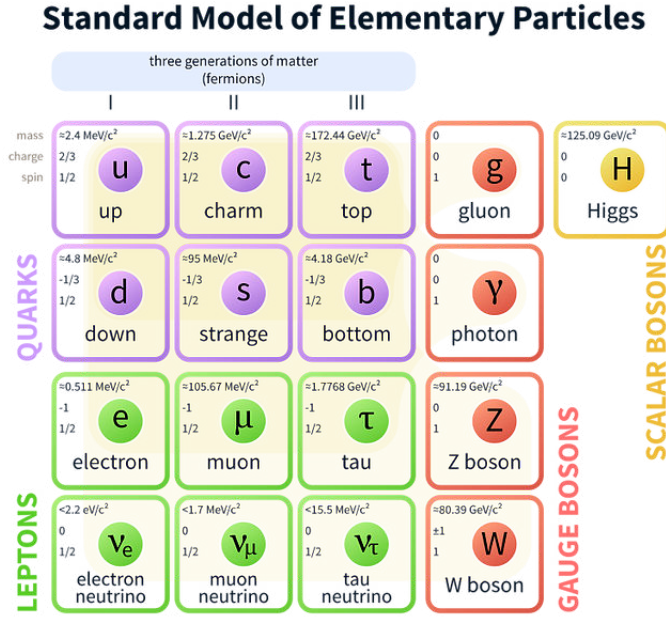


**Figure 2.1:** Schematic representation of the Standard model of particle physics. SM is a theoretical model intended to describe three of the four fundamental forces of the universe in terms of a set of particles and their interactions. [7].

169 that is invariant under a group of transformations a conservation law is expected. For  
 170 instance, a system described by a time-independent Lagrangian is invariant (symmet-  
 171 ric) under time changes (transformations) with the total energy conservation law as  
 172 the expected conservation law. In QED, the charge operator ( $Q$ ) is the generator of  
 173 the  $U(1)$  symmetry which according to the Noether's theorem means that there is a  
 174 conserved quantity; this conserved quantity is the electric charge and thus the law  
 175 conservation of electric charge is established.

176

177 In the SM, the symmetry group  $SU(3)_C \otimes SU(2)_L \otimes U(1)_Y$  describes three of the  
 178 four fundamental interactions in nature(see section 2.2.2): strong interaction(SI),  
 179 weak interaction(WI) and electromagnetic interactions (EI) in terms of symmetries  
 180 associated to physical quantities:

- 181        • Strong:  $SU(3)_C$  associated to color charge
- 182        • Weak:  $SU(2)_L$  associated to weak isospin and chirality
- 183        • Electromagnetic:  $U(1)_Y$  associated to weak hypercharge and electric charge
- 184     It will be shown that the electromagnetic and weak interactions are combined in
- 185     the so-called electroweak interaction where chirality, hypercharge, weak isospin and
- 186     electric charge are the central concepts.

187 **2.2.1 Fermions**

188 The basic constituents of the ordinary matter at the lowest level, which form the set

189 of elementary particles in the SM formulation, are quarks and leptons. All of them

190 have spin 1/2, therefore they are classified as fermions since they obey Fermi-Dirac

191 statistics. There are six “flavors” of quarks and three of leptons organized in three

192 generations, or families, as shown in table 2.1.

193

		Generation		
		1st	2nd	3rd
Leptons	Charged	Electron (e)	Moun( $\mu$ )	Tau ( $\tau$ )
	Neutral	Electron neutrino ( $\nu_e$ )	Muon neutrino ( $\nu_\mu$ )	Tau neutrino ( $\nu_\tau$ )
Quarks	Up-type	Up (u)	Charm (c)	Top (t)
	Down-type	Down (d)	Strange (s)	Bottom (b)

**Table 2.1:** Fermions of the SM. There are six flavors of quarks and three of leptons, organized in three generations, or families, composed of two pairs of closely related particles. The close relationship is motivated by the fact that WI between leptons is limited to the members of the same generation; WI between quarks is not limited but greatly favoured, to same generation members.

194

195 There is a mass hierarchy between generations (see table 2.2), where the higher gener-

196 ation particles decays to the lower one, which can explain why the ordinary matter is

197 made of particles in the first generation. In the SM, neutrinos are modeled as massless  
 198 particles so they are not subject to this mass hierarchy; however, today it is known  
 199 that neutrinos are massive so the hierarchy could be restated. The reason behind this  
 200 mass hierarchy is one of the most important open questions in particle physics, and  
 201 it becomes more puzzling when noticing that the mass difference between first and  
 202 second generation fermions is small compared to the mass difference with respect to  
 203 the third generation.

Lepton	Mass (MeV/c <sup>2</sup> )	Quark	Mass (MeV/c <sup>2</sup> )
e	0.51	u	2.2
$\mu$	105.65	c	$1.28 \times 10^3$
$\tau$	1776.86	t	$173.1 \times 10^3$
$\nu_e$	Unknown	d	4.7
$\nu_\mu$	Unknown	s	96
$\tau_\mu$	Unknown	b	$4.18 \times 10^3$

**Table 2.2:** Fermion masses [9]. Generations differ by mass in a way that have been interpreted as a masss hierarchy. Approximate values with no uncertainties are used, for comparison purpose.

204

205 Usually, the second and third generation fermions are produced in high energy pro-  
 206 cesses, like the ones recreated in particle accelerators.

207 **2.2.1.1 Leptons**

208 A lepton is an elementary particle that is not subject to the SI. As seen in table 2.1,  
 209 there are two types of leptons, the charged ones (electron, muon and tau) and the  
 210 neutral ones (the three neutrinos). The electric charge (Q) is the property that gives  
 211 leptons the ability to participate in the EI. From the classical point of view, Q plays  
 212 a central role determining, among others, the strength of the electric field through  
 213 which the electromagnetic force is exerted. It is clear that neutrinos are not affected

214 by EI because they don't carry electric charge.

215

216 Another feature of the leptons that is fundamental in the mathematical description  
217 of the SM is the chirality, which is closely related to spin and helicity. Helicity defines  
218 the handedness of a particle by relating its spin and momentum such that if they  
219 are parallel then the particle is right-handed; if spin and momentum are antiparallel  
220 the particle is said to be left-handed. The study of parity conservation (or viola-  
221 tion) in  $\beta$ -decay has shown that only left-handed electrons/neutrinos or right-handed  
222 positrons/anti-neutrinos are created [10]; the inclusion of that feature in the theory  
223 was achieved by using projection operators for helicity, however, helicity is frame de-  
224 pendent for massive particles which makes it not Lorentz invariant and then another  
225 related attribute has to be used: *chirality*.

226

227 Chirality is a purely quantum attribute which makes it not so easy to describe in  
228 graphical terms but it defines how the wave function of a particle transforms under  
229 certain rotations. As with helicity, there are two chiral states, left-handed chiral (L)  
230 and right-handed chiral (R). In the highly relativistic limit where  $E \approx p \gg m$  helicity  
231 and chirality converge, becoming exactly the same for massless particles.

232

233 In the following, when referring to left-handed (right-handed) it will mean left-handed  
234 chiral (right-handed chiral). The fundamental fact about chirality is that while EI  
235 and SI are not sensitive to chirality, in WI left-handed and right-handed fermions are  
236 treated asymmetrically, such that only left handed fermions and right-handed anti-  
237 fermions are allowed to couple to WI mediators, which is a violation of parity. The  
238 way to translate this statement in a formal mathematical formulation is based on the  
239 isospin symmetry group  $SU(2)_L$ .

240

241 Each generation of leptons is seen as a weak isospin doublet.<sup>3</sup> The left-handed charged  
 242 lepton and its associated left-handed neutrino are arranged in doublets of weak isospin  
 243 T=1/2 while their right-handed partners are singlets:

$$\begin{pmatrix} \nu_l \\ l \end{pmatrix}_L, l_R := \begin{pmatrix} \nu_e \\ e \end{pmatrix}_L, \begin{pmatrix} \nu_\mu \\ \mu \end{pmatrix}_L, \begin{pmatrix} \nu_\tau \\ \tau \end{pmatrix}_L, e_R, \mu_R, \tau_R, \nu_{eR}, \nu_{\mu R}, \nu_{\tau R} \quad (2.1)$$

244 The isospin third component refers to the eigenvalues of the weak isospin operator  
 245 which for doublets is  $T_3 = \pm 1/2$ , while for singlets it is  $T_3 = 0$ . The physical meaning  
 246 of this doublet-singlet arrangement falls in that the WI couples the two particles in  
 247 the doublet by exchanging the interaction mediator while the singlet member is not  
 248 involved in WI. The main properties of the leptons are summarized in table 2.3.

249

250 Altough all three flavor neutrinos have been observed, their masses remain unknown  
 251 and only some estimations have been made [11]. The main reason is that the fla-  
 252 vor eigenstates are not the same as the mass eigenstates which implies that when  
 253 a neutrino is created its mass state is a linear combination of the three mass eigen-  
 254 states and experiments can only probe the squared difference of the masses. The  
 255 Pontecorvo-Maki-Nakagawa-Sakata (PMNS) mixing matrix encode the relationship  
 256 between flavor and mass eigenstates.

257

### 258 2.2.1.2 Quarks

259 Quarks are the basic constituents of protons and neutrons. The way quarks join to  
 260 form bound states, called “hadrons”, is through the SI. Quarks are affected by all the

---

<sup>3</sup> The weak isospin is an analogy of the isospin symmetry in strong interaction where neutron and proton are affected equally by strong force but differ in their charge.

Lepton	Q(e)	$T_3$	$L_e$	$L_\mu$	$L_\tau$	Lifetime (s)
Electron (e)	-1	-1/2	1	0	0	Stable
Electron neutrino( $\nu_e$ )	0	1/2	1	0	0	Unknown
Muon ( $\mu$ )	-1	-1/2	0	1	0	$2.19 \times 10^{-6}$
Muon neutrino ( $\nu_\mu$ )	0	1/2	0	1	0	Unknown
Tau ( $\tau$ )	-1	-1/2	0	0	1	$290.3 \times 10^{-15}$
Tau neutrino ( $\tau_\mu$ )	0	1/2	0	0	1	Unknown

**Table 2.3:** Leptons properties [9]. Q: electric charge,  $T_3$ : weak isospin. Only left-handed leptons and right-handed anti-leptons participate in the WI. Anti-particles with inverted  $T_3$ , Q and lepton number complete the leptons set but are not listed. Right-handed leptons and left-handed anti-leptons, neither listed, form weak isospin singlets with  $T_3 = 0$  and do not take part in the weak interaction.

261 fundamental interactions which means that they carry all the four types of charges:  
262 color, electric charge, weak isospin and mass.

Flavor	Q(e)	$I_3$	$T_3$	B	C	S	T	$B'$	Y	Color
Up (u)	2/3	1/2	1/2	1/3	0	0	0	0	1/3	r,b,g
Charm (c)	2/3	0	1/2	1/3	1	0	0	0	4/3	r,b,g
Top(t)	2/3	0	1/2	1/3	0	0	1	0	4/3	r,b,g
Down(d)	-1/3	-1/2	-1/2	1/3	0	0	0	0	1/3	r,b,g
Strange(s)	-1/3	0	-1/2	1/3	0	-1	0	0	-2/3	r,b,g
Bottom(b)	-1/3	0	-1/2	1/3	0	0	0	-1	-2/3	r,b,g

**Table 2.4:** Quarks properties [9]. Q: electric charge,  $I_3$ : isospin,  $T_3$ : weak isospin, B: baryon number, C: charmness, S: strangeness, T: topness,  $B'$ : bottomness, Y: hypercharge. Anti-quarks posses the same mass and spin as quarks but all charges (color, flavor numbers) have opposite sign.

263  
264 Table 2.4 summarizes the features of quarks, among which the most particular is  
265 their fractional electric charge. Note that fractional charge is not a problem, given  
266 that quarks are not found isolated, but serves to explain how composed particles are  
267 formed out of two or more valence quarks<sup>4</sup>.  
268

---

<sup>4</sup> Hadrons can contain an indefinite number of virtual quarks and gluons, known as the quark and gluon sea, but only the valence quarks determine hadrons' quantum numbers.

269 Color charge is the responsible for the SI between quarks and is the symmetry  
 270 ( $SU(3)_C$ ) that defines the formalism to describe SI. There are three colors: red (r),  
 271 blue(b) and green(g) and their corresponding three anti-colors; thus each quark carries  
 272 one color unit while anti-quarks carries one anti-color unit. As said above, quarks are  
 273 not allowed to be isolated due to the color confinement effect, therefore their features  
 274 have been studied indirectly by observing their bound states created when:

- 275     • one quark with a color charge is attracted by an anti-quark with the correspond-  
 276         ing anti-color charge forming a colorless particle called a “meson.”
- 277     • three quarks (anti-quarks) with different color (anti-color) charges are attracted  
 278         among them forming a colorless particle called a “baryon(anti-baryon).”

279 In the first version of the quark model (1964), M. Gell-Mann [12] and G. Zweig  
 280 [13, 14] developed a consistent way to classify hadrons according to their properties.  
 281 Only three quarks (u, d, s) were involved in a scheme in which all baryons have  
 282 baryon number  $B=1$  and therefore quarks have  $B=1/3$ ; non-baryons have  $B=0$ . The  
 283 scheme organizes baryons in a two-dimensional space ( $I_3 - Y$ );  $Y$  (hypercharge) and  $I_3$   
 284 (isospin) are quantum numbers related by the Gell-Mann-Nishijima formula [15, 16]:

$$Q = I_3 + \frac{Y}{2} \quad (2.2)$$

285 where  $Y = B + S + C + T + B'$  are the quantum numbers listed in table 2.4. Baryon  
 286 number is conserved in SI and EI which means that single quarks cannot be created  
 287 but in pairs  $q - \bar{q}$ .

288

289 There are six quark flavors organized in three generations (see table 2.1) following a  
 290 mass hierarchy which, again, implies that higher generations decay to first generation

291 quarks.

	Quarks			$T_3$	$Y_W$	Leptons			$T_3$	$Y_W$
Doublets	$(\frac{u}{d'})_L$	$(\frac{c}{s'})_L$	$(\frac{t}{b'})_L$	$(\frac{1/2}{-1/2})$	$1/3$	$(\nu_e)_L$	$(\nu_\mu)_L$	$(\nu_\tau)_L$	$(\frac{1/2}{-1/2})$	$-1$
Singlets	$u_R$	$c_R$	$t_R$	$0$	$4/3$	$\nu_{eR}$	$\nu_{\mu R}$	$\nu_{\tau R}$	$0$	$-2$
	$d'_R$	$s'_R$	$b'_R$	$0$	$-2/3$	$e_R$	$\mu_R$	$\tau_R$		

**Table 2.5:** Fermion weak isospin and weak hypercharge multiplets. Weak hypercharge is calculated through the Gell-Mann-Nishijima formula 2.2 but using the weak isospin and charge for quarks.

292

293 Isospin doublets of quarks are also defined (see table 2.5) and as for neutrinos, the  
 294 mass eigenstates are not the same as the WI eigenstates which means that members of  
 295 different quark generations are connected by the WI mediator; thus, up-type quarks  
 296 are coupled not to down-type quarks directly but to a superposition of down-type  
 297 quarks ( $q'_d$ ) via WI according to:

$$298 \quad q'_d = V_{CKM} q_d$$

$$\begin{pmatrix} d' \\ s' \\ b' \end{pmatrix} = \begin{pmatrix} V_{ud} & V_{us} & V_{ub} \\ V_{cd} & V_{cs} & V_{cb} \\ V_{td} & V_{ts} & V_{tb} \end{pmatrix} \begin{pmatrix} d \\ s \\ b \end{pmatrix} \quad (2.3)$$

299 where  $V_{CKM}$  is known as Cabibbo-Kobayashi-Maskawa (CKM) mixing matrix [17,18].  
 300 The weak decays of quarks are represented in the diagram of figure 2.2; again the  
 301 CKM matrix plays a central role since it contains the probabilities for the different  
 302 quark decay channels, in particular, note that quark decays are greatly favored be-  
 303 tween generation members.

304

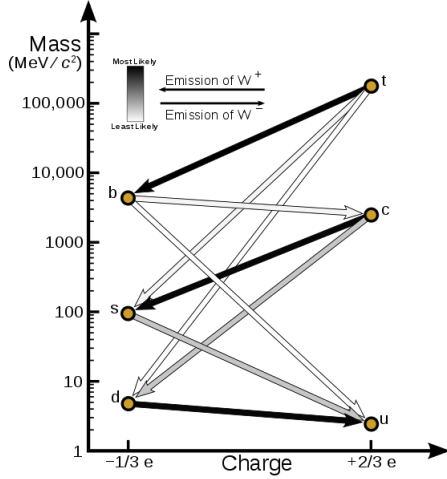


**Figure 2.2:** Transformations between quarks through the exchange of a WI. Higher generations quarks decay to first generation quarks by emitting a W boson. The arrow color indicates the likelihood of the transition according to the grey scale in the top left side which represent the CKM matrix parameters [19].

305 CKM matrix is a  $3 \times 3$  unitary matrix parametrized by three mixing angles and  
 306 the *CP-mixing phase*; the latter is the parameter responsible for the Charge-Parity  
 307 symmetry violation (CP-violation) in the SM. The fact that the b quark decays almost  
 308 all the times to a top quark is exploited in this thesis when making the selection of  
 309 the signal events by requiring the presence of a jet tagged as a jet coming from a  
 310 b quark in the final state. The effect of the *CP-mixing phase* on the cross section of  
 311 associated production of Higgs boson and a single top process is also explored in this  
 312 thesis.

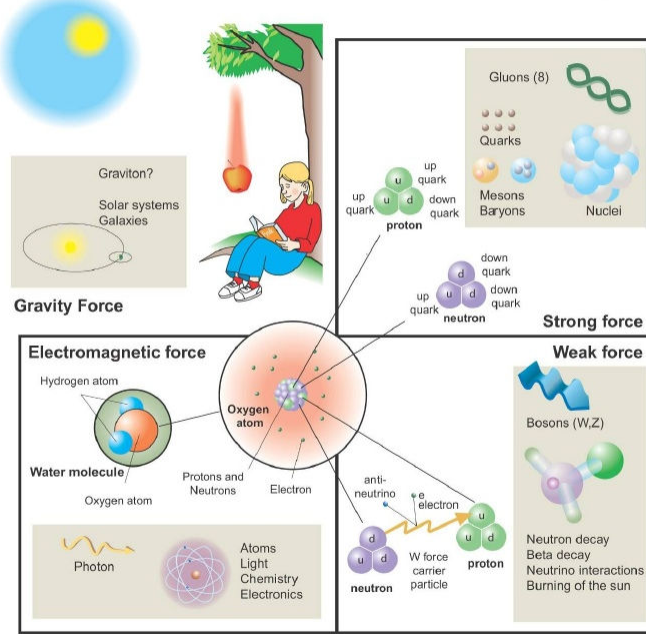
### 313 2.2.2 Fundamental interactions

314 Even though there are many manifestations of force in nature, like the ones repre-  
 315 sented in figure 2.3, we can classify all of them into one of four fundamental interac-  
 316 tions:

- 317 • *Electromagnetic interaction (EI)* affects particles that are “electrically charged,”

## Fundamental interactions.

Illustration: Typoform



Summer School KPI 15 August 2009

**Figure 2.3:** Fundamental interactions in nature. Despite the many manifestations of forces in nature, we can track all of them back to one of the fundamental interactions. The most common forces are gravity and electromagnetic given that all of us are subject and experience them in everyday life.

318 like electrons and protons. It is described by QED combining quantum mechan-  
 319 ics, special relativity and electromagnetism in order to explain how particles  
 320 with electric charge interact through the exchange of photons, therefore, one  
 321 says that “Electromagnetic Force” is mediated by “photons”. Figure 2.4a. shows  
 322 a graphical representation, known as “feynman diagram”, of electron-electron  
 323 scattering.

- 324 • *Strong interaction (SI)* described by Quantum Chromodynamics (QCD). Hadrons  
 325 like proton and neutron have internal structure given that they are composed  
 326 of two or more valence quarks<sup>5</sup>. Quarks have fractional electric charge which  
 327 means that they are subject to electromagnetic interaction and in the case of the

<sup>5</sup> particles made of four and five quarks are exotic states not so common.

328 proton they should break apart due to electrostatic repulsion; however, quarks  
 329 are held together inside the hadrons against their electrostatic repulsion by the  
 330 “Strong Force” through the exchange of “gluons.” The analog to the electric  
 331 charge is the “color charge”. Electrons and photons are elementary particles  
 332 as quarks but they don’t carry color charge, therefore they are not subject to  
 333 SI. The feynman diagram for gluon exchange between quarks is shown in figure  
 334 2.4b.

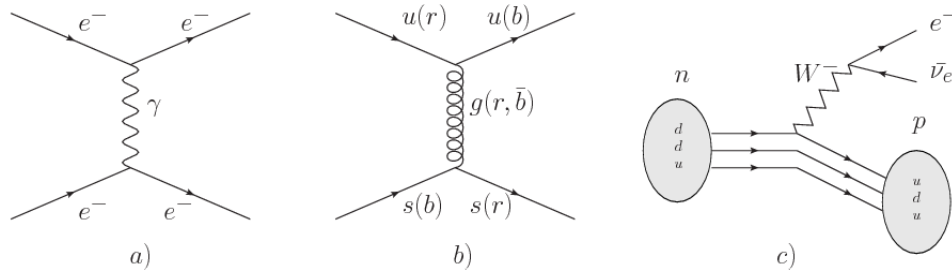


**Figure 2.4:** Feynman diagrams representing the interactions in SM; a) EI:  $e$ - $e$  scattering; b) SI: gluon exchange between quarks ; c) WI:  $\beta$ -decay

335 • *Weak interaction (WI)* described by the weak theory (WT), is responsible, for  
 336 instance, for the radioactive decay in atoms and proton-proton (pp) fusion  
 337 within the sun. Quarks and leptons are the particles affected by the weak  
 338 interaction; they possess a property called “flavor charge” (see 2.2.1) which can  
 339 be changed by emitting or absorbing one weak force mediator. There are three  
 340 mediators of the “weak force” known as “Z” boson in the case of electrically  
 341 neutral changes and “ $W^\pm$ ” bosons in the case of electrically charged changes.  
 342 The “weak isospin” is the WI analog to electric charge in EI, and color charge  
 343 in SI, and defines how quarks and leptons are affected by the weak force. Figure  
 344 2.4c. shows the feynman diagram of  $\beta$ -decay where a newtron (n) is transformed  
 345 in a proton (p) by emmiting a  $W^-$  particle. Since this thesis is in the frame  
 346 of the electroweak interaction, a more detailed description of it will be given in

347 section 2.3

- 348 • *Gravitational interaction (GI)* described by General Theory of Relativity (GR).  
 349 It is responsible for the structure of galaxies and black holes as well as the  
 350 expansion of the universe. As a classical theory, in the sense that it can be for-  
 351 mulated without even appeal to the concept of quantization, it implies that the  
 352 spacetime is a continuum and predictions can be made without limitation to the  
 353 precision of the measurement tools. The latter represent a direct contradic-  
 354 tion of the quantum mechanics principles. Gravity is deterministic while quantum  
 355 mechanics is probabilistic; despite that, efforts to develop a quantum theory of  
 356 gravity have predicted the “graviton” as mediator of the Gravitational force<sup>6</sup>.

Interaction	Acts on	Relative strength	Range (m)	Mediators
Electromagnetic (QED)	Electrically charged particles	$10^{-2}$	Infinite	Photon
Strong (QCD)	Quarks and gluons	1	$10^{-15}$	Gluon
Weak (WI)	Leptons and quarks	$10^{-6}$	$10^{-18}$	$W^\pm, Z$
Gravitational (GI)	Massive particles	$10^{-39}$	Infinite	Graviton

**Table 2.6:** Fundamental interactions features [20].

357

358 Table 2.6 summarizes the main features of the fundamental interactions. The rela-  
 359 tive strength of the fundamental forces reveals the meaning of strong and weak; in  
 360 a context where the relative strength of the SI is 1, the EI is about hundred times  
 361 weaker and WI is about million times weaker than the SI. A good description on  
 362 how the relative strength and range of the fundamental interactions are calculated  
 363 can be found in references [20, 21]. In the everyday life, only EI and GI are explicitly  
 364 experienced due to the range of these interactions; i.e., at the human scale distances

---

<sup>6</sup> Actually a wide variety of theories have been developed in an attempt to describe gravity; some famous examples are string theory and supergravity.

365 only EI and GI have appreciable effects, in contrast to SI which at distances greater  
 366 than  $10^{-15}$ m become negligible.

367

368 QED was built successfully on the basis of the classical electrodynamics theory (CED)  
 369 of Maxwell and Lorentz, following theoretical and experimental requirements imposed  
 370 by

- 371     • lorentz invariance: independence on the reference frame.
- 372     • locallity: interacting fields are evaluated at the same space-time point to avoid  
     373       action at a distance.
- 374     • renormalizability: physical predictions are finite and well defined
- 375     • particle spectrum, symmetries and conservation laws already known must emerge  
     376       from the theory.
- 377     • gauge invariance.

378 The gauge invariance requirement reflects the fact that the fundamental fields cannot  
 379 be directly measured but associated fields which are the observables. Electric (“**E**”)  
 380 and magnetic (“**B**”) fields in CED are associated with the electric scalar potential  
 381 “**V**” and the vector potential “**A**”. In particular, **E** can be obtained by measuring  
 382 the change in the space of the scalar potential ( $\Delta V$ ); however, two scalar potentials  
 383 differing by a constant “f” correspond to the same electric field. The same happens in  
 384 the case of the vector potential “**A**”; thus, different configurations of the associated  
 385 fields result in the same set of values of the observables. The freedom in choosing  
 386 one particular configuration is known as “gauge freedom”; the transformation law con-  
 387 necting two configurations is known as “gauge transformation” and the fact that the

388 observables are not affected by a gauge transformation is called “gauge invariance”.

389

390 When the gauge transformation:

$$\begin{aligned}\mathbf{A} &\rightarrow \mathbf{A} - \nabla f \\ V &\rightarrow V - \frac{\partial f}{\partial t}\end{aligned}\tag{2.4}$$

391 is applied to Maxwell equations, they are still satisfied and the fields remain invariant.

392 Thus, CED is invariant under gauge transformations and is called a “gauge theory”.

393 The set of all gauge transformations form the “symmetry group” of the theory, which

394 according to the group theory, has a set of “group generators”. The number of group

395 generators determine the number of “gauge fields” of the theory.

396

397 As mentioned in the first lines of section 2.2, QED has one symmetry group ( $U(1)$ )

398 with one group generator (the  $Q$  operator) and one gauge field (the electromagnetic

399 field  $A^\mu$ ). In CED there is not a clear definition, beyond the historical convention, of

400 which fields are the fundamental and which are the associated, but in QED it is clear

401 that the fundamental field is  $A^\mu$ . When a gauge theory is quantized, the gauge field

402 is quantized and its quanta is called “gauge boson”. The word boson characterizes

403 particles with integer spin which obvey Bose-einstein statistics.

404

405 As will be detailed in section 2.3, interactions between particles in a system can be

406 obtained by considering first the Lagrangian density of free particles in the system,

407 which of course is incomplete because the interaction terms have been left out, and

408 demanding global phase transformation invariance. Global phase transformation in-

409 variance means that a gauge transformation is performed identically to every point  
 410 in the space<sup>7</sup> and the Lagrangian remains invariant. Then, the global transformation  
 411 is promoted to a local phase transformation (this time the gauge transformation de-  
 412 pends on the position in space) and again invariance is required.

413

414 Due to the space dependence of the local tranformation, the Lagrangian density is  
 415 not invariant anymore. In order to restate the gauge invariance, the gauge covariant  
 416 derivative is introduced in the Lagrangian and with it the gauge field responsible for  
 417 the interaction between particles in the system. The new Lagrangian density is gauge  
 418 invariant, includes the interaction terms needed to account for the interactions and  
 419 provides a way to explain the interaction between particles through the exchange of  
 420 the gauge boson.

421 This recipe was used to build QED and the theories that aim to explain the funda-  
 422 mental interactions.

### 423 **2.2.3 Gauge bosons**

424 The importance of the gauge bosons comes from the fact that they are the force  
 425 mediators or force carriers. The features of the gauge bosons reflect those of the  
 426 fields they represent and they are extracted from the Lagrangian density used to  
 427 describe the interactions. In section 2.3, it will be shown how the gauge bosons of the  
 428 EI and WI emerge from the electroweak Lagrangian. The SI gauge bosons features  
 429 are also extracted from the SI Lagrangian but it is not detailed in this document. The  
 430 main features of the SM gauge bosons will be briefly presented below and summarized  
 431 in table 2.7.

---

<sup>7</sup> Here space corresponds to the 4-dimensional space i.e. space-time.

- 432     • **Photon.** EI occurs when the photon couples to (is exchanged between) particles  
 433       carrying electric charge; however, the photon itself does not carry electric charge,  
 434       therefore, there is no coupling between photons. Given that the photon is  
 435       massless the EI is of infinite range, i.e., electrically charged particles interact  
 436       even if they are located far away one from each other; this also implies that  
 437       photons always move with the speed of light.
- 438     • **Gluon.** SI is mediated by gluons which, same as photons, are massless. They  
 439       carry one unit of color charge and one unit of anticolor charge which means that  
 440       gluons couple to other gluons. As a result, the range of the SI is not infinite  
 441       but very short due to the attraction between gluons, giving rise to the “color  
 442       confinement” which explains why color charged particles cannot be isolated but  
 443       live within composited particles, like quarks inside protons.
- 444     • **W, Z.** The WI mediators,  $W^\pm$  and Z, are massive which explains their short-  
 445       range. Given that the WI is the only interaction that can change the flavor  
 446       of the interacting particles, the W boson is the responsible for the nuclear  
 447       transmutation where a neutron is converted in a proton or vice versa with the  
 448       involvement of an electron and a neutrino (see figure 2.4c). The Z boson is the  
 449       responsible of the neutral weak processes like neutrino elastic scattering where  
 450       no electric charge but momentum transference is involved. WI gauge bosons  
 451       carry isospin charge which makes possible the interaction between them.

Interaction	Mediator	Electric charge (e)	Color charge	Weak Isospin	mass (GeV/c <sup>2</sup> )
Electromagnetic	Photon ( $\gamma$ )	0	No	0	0
Strong	Gluon (g)	0	Yes -octet	No	0
Weak	$W^\pm$	$\pm 1$	No	$\pm 1$	$80.385 \pm 0.015$
	Z	0	No	0	$91.188 \pm 0.002$

Table 2.7: SM gauge bosons main features [9].

## 453 2.3 Electroweak unification and the Higgs

### 454 mechanism

455 Physicists dream of building a theory that contains all the interactions in one single  
 456 interaction, i.e., showing that at some scale in energy all the four fundamental in-  
 457 teractions are unified and only one interaction emerges in a “Theory of everything”.  
 458 The first sign of the feasibility of such unification comes from success in the con-  
 459 struction of the CED. Einstein spent years trying to reach that dream, which by  
 460 1920 only involved electromagnetism and gravity, with no success; however, a new  
 461 partial unification was achieved in the 1960’s, when S.Glashow [22], A.Salam [23] and  
 462 S.Weinberg [24] independently proposed that electromagnetic and weak interactions  
 463 are two manifestations of a more general interaction called “electroweak interaction  
 464 (EWT)”. Both, QCD and EWT, were developed in parallel and following the useful  
 465 prescription provided by QED and the gauge invariance principles.

466

467 The theory of weak interactions was capable of explaining the  $\beta$ -decay and in general  
 468 the processes mediated by  $W^\pm$  bosons. However, there were some processes like the  
 469 “ $\nu_\mu - e$  scattering” which would require the exchange of two W bosons (see figure 2.5  
 470 top diagrams) giving rise to divergent loop integrals and then non finite predictions.  
 471 By including neutral currents involving fermions via the exchange of neutral bosons  
 472 Z, those divergences are compensated and the predictions become realistic.

473

474 Neutral weak interaction vertices conserve flavor in the same way as the electromag-  
 475 netic vertices do, but additionally, the Z boson can couple to neutrinos which implies  
 476 that processes involving charged fermions can proceed through EI or WI but processes  
 477 involving neutrinos can proceed only through WI.

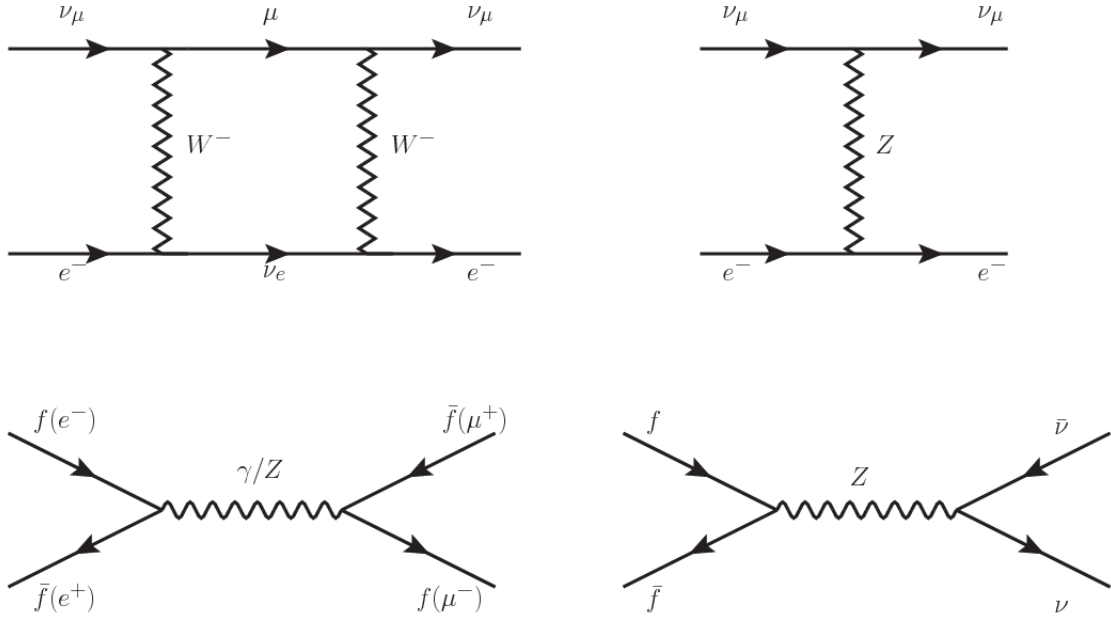


**Figure 2.5:** Top:  $\nu_\mu - e^-$  scattering going through charged currents (left) and neutral currents (right). Bottom: neutral current processes for charged fermions (left) and involving neutrinos (right). While neutral current processes involving only charged fermions can proceed through EI or WI, those involving neutrinos can only proceed via WI.

478

479 The prescription to build a gauge theory of the WI consists of proposing a free field  
480 Lagrangian density that includes the particles involved; next, by requesting invari-  
481 ance under global phase transformations first and generalizing to local phase trans-  
482 formations invariance later, the conserved currents are identified and interactions are  
483 generated by introducing gauge fields. Given that the goal is to include the EI and  
484 WI in a single theory, the group symmetry considered should be a combination of  
485  $SU(2)_L$  and  $U(1)_{em}$ , however the latter cannot be used directly because the EI treats  
486 left and right-handed particles indistinctly in contrast to the former. Fortunately, the  
487 weak hypercharge, which is a combination of the weak isospin and the electric charge  
488 (eqn 2.2) is suitable to be used since it is conserved by the EI and WI. Thus, the  
489 symmetry group to be considered is

$$G \equiv SU(2)_L \otimes U(1)_Y \quad (2.5)$$

490 The following treatment applies to any of the fermion generations, but for simplicity  
 491 the first generation of leptons will be considered [5, 6, 25, 26].

492

493 Given the first generation of leptons

$$\psi_1 = \begin{pmatrix} \nu_e \\ e^- \end{pmatrix}_L, \quad \psi_2 = \nu_{eR}, \quad \psi_3 = e_R^- \quad (2.6)$$

494 the charged fermionic currents are given by

$$J_\mu \equiv J_\mu^+ = \bar{\nu}_{eL} \gamma_\mu e_L, \quad J_\mu^\dagger \equiv J_\mu^- = \bar{e}_L \gamma_\mu \nu_{eL} \quad (2.7)$$

495 and the free Lagrangian is given by

$$\mathcal{L}_0 = \sum_{j=1}^3 i\bar{\psi}_j(x) \gamma^\mu \partial_\mu \psi_j(x). \quad (2.8)$$

496 Mass terms are included directly in the QED and QCD free Lagrangians since they  
 497 preserve the invariance under the symmetry transformations involved which treat  
 498 left-handed and right-handed similarly, however mass terms of the form

$$m_W^2 W_\mu^\dagger(x) W^\mu(x) + \frac{1}{2} m_Z^2 Z_\mu(x) Z^\mu(x) - m_e \bar{\psi}_e(x) \psi_e(x) \quad (2.9)$$

499 which represent the mass of  $W^\pm$ , Z and electrons, are not invariant under G trans-  
 500 formations, therefore the gauge fields described by the EWI are in principle massless.

501

502 Experiments have shown that the gauge fields are not massless; however, they have

503 to acquire mass through a mechanism compatible with the gauge invariance; that  
 504 mechanism is known as the “Higgs mechanism” and will be considered later in this  
 505 section. The global transformations in the combined symmetry group  $G$  can be  
 506 written as

$$\begin{aligned}\psi_1(x) &\xrightarrow{G} \psi'_1(x) \equiv U_Y U_L \psi_1(x), \\ \psi_2(x) &\xrightarrow{G} \psi'_2(x) \equiv U_Y \psi_2(x), \\ \psi_3(x) &\xrightarrow{G} \psi'_3(x) \equiv U_Y \psi_3(x)\end{aligned}\tag{2.10}$$

507 where  $U_L$  represent the  $SU(2)_L$  transformation acting only on the weak isospin dou-  
 508 blet and  $U_Y$  represent the  $U(1)_Y$  transformation acting on all the weak isospin mul-  
 509 tiplets. Explicitly

$$U_L \equiv \exp\left(i\frac{\sigma_i}{2}\alpha^i\right), \quad U_Y \equiv \exp(iy_i\beta) \quad (i = 1, 2, 3)\tag{2.11}$$

510 with  $\sigma_i$  the Pauli matrices and  $y_i$  the weak hypercharges. In order to promote the  
 511 transformations from global to local while keeping the invariance, it is required that  
 512  $\alpha^i = \alpha^i(x)$ ,  $\beta = \beta(x)$  and the replacement of the ordinary derivatives by the covariant  
 513 derivatives

$$\begin{aligned}D_\mu \psi_1(x) &\equiv [\partial_\mu + ig\sigma_i W_\mu^i(x)/2 + ig'y_1 B_\mu(x)] \psi_1(x) \\ D_\mu \psi_2(x) &\equiv [\partial_\mu + ig'y_2 B_\mu(x)] \psi_2(x) \\ D_\mu \psi_3(x) &\equiv [\partial_\mu + ig'y_3 B_\mu(x)] \psi_3(x)\end{aligned}\tag{2.12}$$

514 introducing in this way four gauge fields,  $W_\mu^i(x)$  and  $B_\mu(x)$ , in the process. The  
 515 covariant derivatives (eqn 2.12) are required to transform in the same way as fermion  
 516 fields  $\psi_i(x)$  themselves, therefore, the gauge fields transform as:

$$\begin{aligned} B_\mu(x) &\xrightarrow{G} B'_\mu(x) \equiv B_\mu(x) - \frac{1}{g'} \partial_\mu \beta(x) \\ W_\mu^i(x) &\xrightarrow{G} W_\mu^{i\prime}(x) \equiv W_\mu^i(x) - \frac{i}{g} \partial_\mu \alpha_i(x) - \varepsilon_{ijk} \alpha_i(x) W_\mu^j(x). \end{aligned} \quad (2.13)$$

517 The G invariant version of the Lagrangian density 2.8 can be written as

$$\mathcal{L}_0 = \sum_{j=1}^3 i \bar{\psi}_j(x) \gamma^\mu D_\mu \psi_j(x) \quad (2.14)$$

518 where free massless fermion and gauge fields and fermion-gauge boson interactions  
 519 are included. The EWI Lagrangian density must additionally include kinetic terms  
 520 for the gauge fields ( $\mathcal{L}_G$ ) which are built from the field strengths, according to

$$B_{\mu\nu}(x) \equiv \partial_\mu B_\nu - \partial_\nu B_\mu \quad (2.15)$$

$$W_{\mu\nu}^i(x) \equiv \partial_\mu W_\nu^i(x) - \partial_\nu W_\mu^i(x) - g \varepsilon^{ijk} W_\mu^j W_\nu^k \quad (2.16)$$

521 the last term in eqn. 2.16 is added in order to hold the gauge invariance; therefore,

$$\mathcal{L}_G = -\frac{1}{4} B_{\mu\nu}(x) B^{\mu\nu}(x) - \frac{1}{4} W_{\mu\nu}^i(x) W_i^{\mu\nu}(x) \quad (2.17)$$

522 which contains not only the free gauge fields contributions, but also the gauge fields  
 523 self-interactions and interactions among them.

525 The three weak isospin conserved currents resulting from the  $SU(2)_L$  symmetry are  
 526 given by

$$J_\mu^i(x) = \frac{1}{2} \bar{\psi}_1(x) \gamma_\mu \sigma^i \psi_1(x) \quad (2.18)$$

527 while the weak hypercharge conserved current resulting from the  $U(1)_Y$  symmetry is  
 528 given by

$$J_\mu^Y = \sum_{j=1}^3 \bar{\psi}_j(x) \gamma_\mu y_j \psi_j(x) \quad (2.19)$$

529 In order to evaluate the electroweak interactions modeled by an isovector field  $W_\mu^i$   
 530 which couples to isospin currents  $J_\mu^i$  with strength  $g$  and additionally the singlet  
 531 field  $B_\mu$  which couples to the weak hypercharge current  $J_\mu^Y$  with strength  $g'/2$ . The  
 532 interaction Lagrangian density to be considered is

$$\mathcal{L}_I = -g J^{i\mu}(x) W_\mu^i(x) - \frac{g'}{2} J^{Y\mu}(x) B_\mu(x) \quad (2.20)$$

533 Note that the weak isospin currents are not the same as the charged fermionic currents  
 534 that were used to describe the WI (eqn 2.7), since the weak isospin eigenstates are  
 535 not the same as the mass eigenstates, but they are closely related

$$J_\mu = \frac{1}{2} (J_\mu^1 + i J_\mu^2), \quad J_\mu^\dagger = \frac{1}{2} (J_\mu^1 - i J_\mu^2). \quad (2.21)$$

536 The same happens with the gauge fields  $W_\mu^i$  which are related to the mass eigenstates  
 537  $W^\pm$  by

$$W_\mu^+ = \frac{1}{\sqrt{2}} (W_\mu^1 - i W_\mu^2), \quad W_\mu^- = \frac{1}{\sqrt{2}} (W_\mu^1 + i W_\mu^2). \quad (2.22)$$

538 The fact that there are three weak isospin conserved currents is an indication that in  
 539 addition to the charged fermionic currents, which couple charged to neutral leptons,  
 540 there should be a neutral fermionic current that does not involve electric charge  
 541 exchange; therefore, it couples neutral fermions or fermions of the same electric charge.  
 542 The third weak isospin current contains a term that is similar to the electromagnetic  
 543 current ( $j_\mu^{em}$ ), indicating that there is a relation between them and resembling the  
 544 Gell-Mann-Nishijima formula 2.2 adapted to electroweak interactions

$$Q = T_3 + \frac{Y_W}{2}. \quad (2.23)$$

545 Just as  $Q$  generates the  $U(1)_{em}$  symmetry, the weak hypercharge generates the  $U(1)_Y$   
 546 symmetry as said before. It is possible to write the relationship in terms of the currents  
 547 as

$$j_\mu^{em} = J_\mu^3 + \frac{1}{2}J_\mu^Y. \quad (2.24)$$

548 The neutral gauge fields  $W_\mu^3$  and  $B_\mu$  cannot be directly identified with the  $Z$  and the  
 549 photon fields since the photon interacts similarly with left and right-handed fermions;  
 550 however, they are related through a linear combination given by

$$\begin{aligned} A_\mu &= B_\mu \cos \theta_W + W_\mu^3 \sin \theta_W \\ Z_\mu &= -B_\mu \sin \theta_W + W_\mu^3 \cos \theta_W \end{aligned} \quad (2.25)$$

551 where  $\theta_W$  is known as the “Weinberg angle.” The interaction Lagrangian is now given

552 by

$$\mathcal{L}_I = -\frac{g}{\sqrt{2}}(J^\mu W_\mu^+ + J^{\mu\dagger} W_\mu^-) - \left(g \sin \theta_W J_\mu^3 + g' \cos \theta_W \frac{J_\mu^Y}{2}\right) A^\mu - \left(g \cos \theta_W J_\mu^3 - g' \sin \theta_W \frac{J_\mu^Y}{2}\right) Z^\mu \quad (2.26)$$

553 the first term is the weak charged current interaction, while the second term is the  
554 electromagnetic interaction under the condition

$$g \sin \theta_W = g' \cos \theta_W = e, \quad \frac{g'}{g} = \tan \theta_W \quad (2.27)$$

555 contained in the eqn.2.24; the third term is the neutral weak current.

556

557 Note that the neutral fields transformation given by the eqn. 2.25 can be written in  
558 terms of the coupling constants  $g$  and  $g'$  as:

$$A_\mu = \frac{g' W_\mu^3 + g B_\mu}{\sqrt{g^2 + g'^2}}, \quad Z_\mu = \frac{g W_\mu^3 - g' B_\mu}{\sqrt{g^2 + g'^2}} \quad (2.28)$$

559 So far, the Lagrangian density describing the non-massive EWI is:

$$\mathcal{L}_{nmEWI} = \mathcal{L}_0 + \mathcal{L}_G \quad (2.29)$$

560 where fermion and gauge fields have been considered massless because their regular  
561 mass terms are manifestly non invariant under G transformations; therefore, masses  
562 have to be generated in a gauge invariant way. The mechanism by which this goal is  
563 achieved is known as the “Higgs mechanism” and is closely connected to the concept  
564 of “spontaneous symmetry breaking.”

### 565 2.3.1 Spontaneous symmetry breaking (SSB)

566 Figure 2.6 left shows a steel nail (top) which is subject to an external force; the form  
 567 of the potential energy is also shown (bottom).

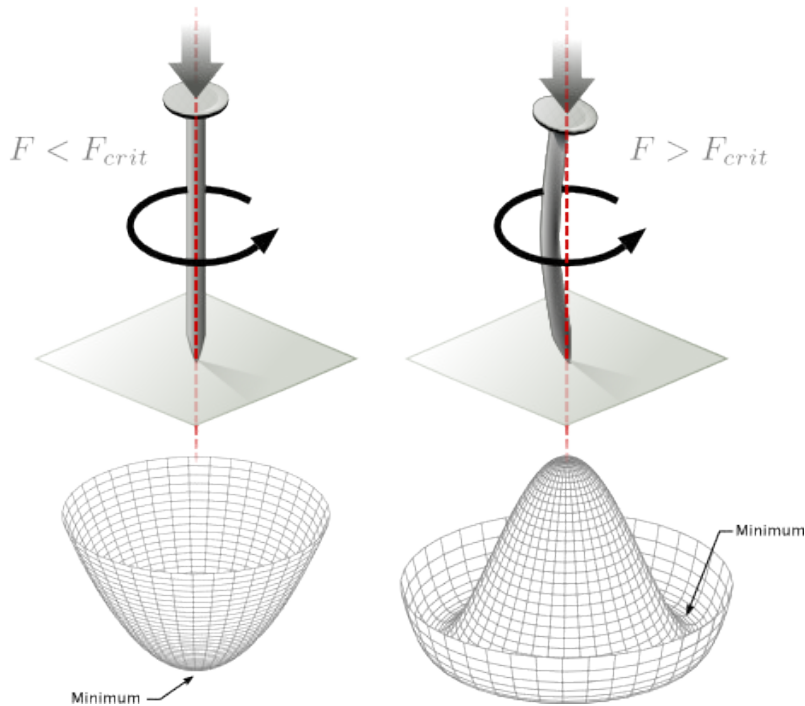


**Figure 2.6:** Spontaneous symmetry breaking mechanism. The steel nail, subject to an external force (top left), has rotational symmetry with respect to its axis. When the external force overcomes a critical value the nail buckles (top right) choosing a minimal energy state (ground state) and thus “*breaking spontaneously the rotational symmetry*”. The potential energy (bottom) changes but holds the rotational symmetry; however, an infinite number of asymmetric ground states are generated and circularly distributed in the bottom of the potential [27].

568

569 Before reaching the critical force value, the system has rotational symmetry with re-  
 570 spect to the nail axis; however, after the critical force value is reached the nail buckles  
 571 (top right). The form of the potential energy (bottom right) changes, preserving its  
 572 rotational symmetry although its minima does not exhibit that rotational symmetry  
 573 any longer. Right before the nail buckles there is no indication of the direction the

574 nail will bend because any of the directions are equivalent, but once the nail bends,  
 575 choosing a direction, an arbitrary minimal energy state (ground state) is selected and  
 576 it does not share the system's rotational symmetry. This mechanism for reaching an  
 577 asymmetric ground state is known as "*spontaneous symmetry breaking*".

578 The lesson from this analysis is that the way to introduce the SSB mechanism into a  
 579 system is by adding the appropriate potential to it.

580

581 Figure 2.7 shows a plot of the potential  $V(\phi)$  in the case of a scalar field  $\phi$

$$V(\phi) = \mu^2 \phi^\dagger \phi + \lambda (\phi^\dagger \phi)^2 \quad (2.30)$$

582 If  $\mu^2 > 0$  the potential has only one minimum at  $\phi = 0$  and describes a scalar field  
 583 with mass  $\mu$ . If  $\mu^2 < 0$  the potential has a local maximum at  $\phi = 0$  and two minima  
 584 at  $\phi = \pm\sqrt{-\mu^2/\lambda}$  which enables the SSB mechanism to work.

585

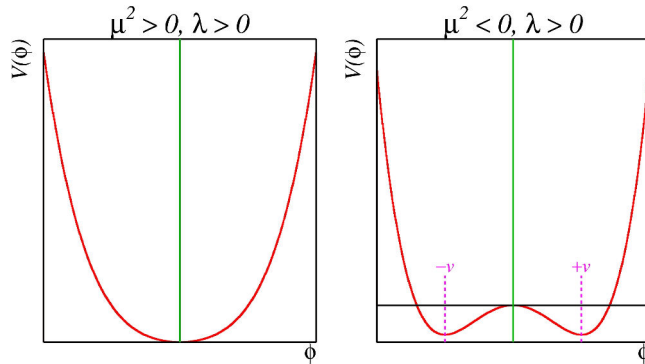


**Figure 2.7:** Shape of the potential  $V(\phi)$  for  $\lambda > 0$  and:  $\mu^2 > 0$  (left) and  $\mu^2 < 0$  (right). The case  $\mu^2 < 0$  corresponds to the potential suitable for introducing the SSB mechanism by choosing one of the two ground states which are connected via reflection symmetry. [27].

586 In the case of a complex scalar field  $\phi(x)$

$$\phi(x) = \frac{1}{\sqrt{2}}(\phi_1 + i\phi_2) \quad (2.31)$$

587 the Lagrangian (invariant under global  $U(1)$  transformations) is given by

$$\mathcal{L} = (\partial_\mu \phi)^\dagger (\partial^\mu \phi) - V(\phi), \quad V(\phi) = \mu^2 \phi^\dagger \phi + \lambda (\phi^\dagger \phi)^2 \quad (2.32)$$

588 where an appropriate potential has been added in order to introduce the SSB.

589

590 As seen in figure 2.8, the potential has now an infinite number of minima circularly  
 591 distributed along the  $\xi$ -direction which makes possible the occurrence of the SSB by  
 592 choosing an arbitrary ground state; for instance,  $\xi = 0$ , i.e.  $\phi_1 = v, \phi_2 = 0$

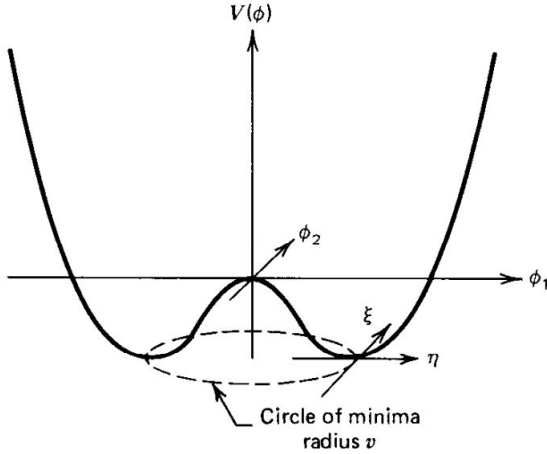


**Figure 2.8:** Potential for complex scalar field. There is a circle of minima of radius  $v$  along the  $\xi$ -direction [6].

$$\phi_0 = \frac{v}{\sqrt{2}} \exp(i\xi) \xrightarrow{SSB} \phi_0 = \frac{v}{\sqrt{2}} \quad (2.33)$$

593 As usual, excitations over the ground state are studied by making an expansion about

594 it; thus, the excitation can be parametrized as:

$$\phi(x) = \frac{1}{\sqrt{2}}(v + \eta(x) + i\xi(x)) \quad (2.34)$$

595 which when substituted into eqn. 2.32 produces a Lagrangian in terms of the new  
596 fields  $\eta$  and  $\xi$

$$\mathcal{L}' = \frac{1}{2}(\partial_\mu\xi)^2 + \frac{1}{2}(\partial_\mu\eta)^2 + \mu^2\eta^2 - V(\phi_0) - \lambda v\eta(\eta^2 + \xi^2) - \frac{\lambda}{4}(\eta^2 + \xi^2)^2 \quad (2.35)$$

597 where the last two terms represent the interactions and self-interaction between the  
598 two fields  $\eta$  and  $\xi$ . The particular feature of the SSB mechanism is revealed when  
599 looking to the first three terms of  $\mathcal{L}'$ . Before the SSB, only the massless  $\phi$  field is  
600 present in the system; after the SSB there are two fields of which the  $\eta$ -field has  
601 acquired mass  $m_\eta = \sqrt{-2\mu^2}$  while the  $\xi$ -field is still massless (see figure 2.9).

602

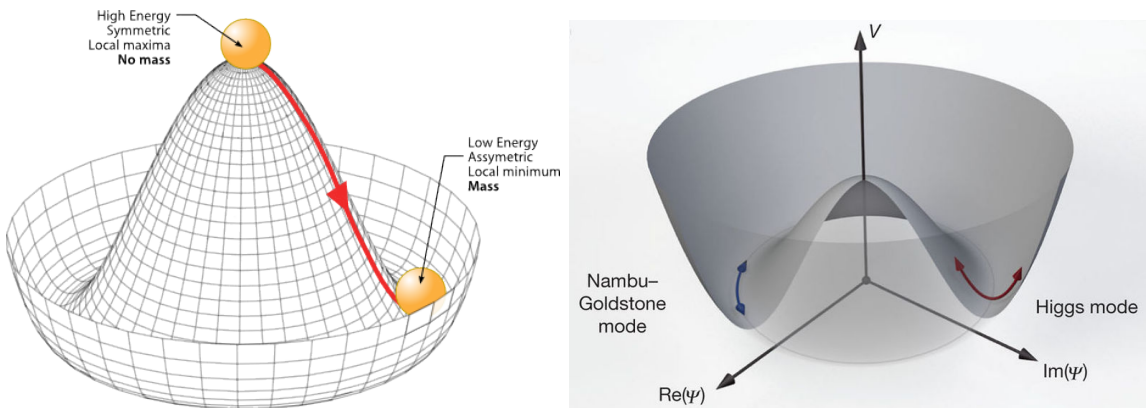


**Figure 2.9:** SSB mechanism for a complex scalar field [27, 28].

603 Thus, the SSB mechanism serves as a method to generate mass but as a side effect a  
604 massless field is introduced in the system. This fact is known as the Goldstone theorem

and states that a massless scalar field appears in the system for each continuous symmetry spontaneously broken. Another version of the Goldstone theorem states that “*if a Lagrangian is invariant under a continuous symmetry group  $G$ , but the vacuum is only invariant under a subgroup  $H \subset G$ , then there must exist as many massless spin-0 particles (Nambu-Goldstone bosons) as broken generators.*” [26] The Nambu-Goldstone boson can be understood considering that the potential in the  $\xi$ -direction is flat so excitations in that direction are not energy consuming and thus represent a massless state.

### 2.3.2 Higgs mechanism

When the SSB mechanism is introduced in the formulation of the EWI in an attempt to generate the mass of the so far massless gauge bosons and fermions, an interesting effect is revealed. In order to keep the  $G$  symmetry group invariance and generate the mass of the EW gauge bosons, a  $G$  invariant Lagrangian density ( $\mathcal{L}_S$ ) has to be added to the non massive EWI Lagrangian (eqn. 2.29)

$$\mathcal{L}_S = (D_\mu \phi)^\dagger (D^\mu \phi) - \mu^2 \phi^\dagger \phi - \lambda (\phi^\dagger \phi)^2, \quad \lambda > 0, \mu^2 < 0 \quad (2.36)$$

$$D_\mu \phi = \left( i\partial_\mu - g \frac{\sigma_i}{2} W_\mu^i - g' \frac{Y}{2} B_\mu \right) \phi \quad (2.37)$$

$\phi$  has to be an isospin doublet of complex scalar fields so it preserves the  $G$  invariance; thus  $\phi$  can be defined as:

$$\phi = \begin{pmatrix} \phi^+ \\ \phi^0 \end{pmatrix} \equiv \frac{1}{\sqrt{2}} \begin{pmatrix} \phi_1 + i\phi_2 \\ \phi_3 + i\phi_4 \end{pmatrix}. \quad (2.38)$$

The minima of the potential are defined by

$$\phi^\dagger \phi = \frac{1}{2}(\phi_1^2 + \phi_2^2 + \phi_3^2 + \phi_4^2) = -\frac{\mu^2}{2\lambda}. \quad (2.39)$$

622 The choice of the ground state is critical. By choosing a ground state, invariant under  
 623  $U(1)_{em}$  gauge symmetry, the photon will remain massless and the  $W^\pm$  and  $Z$  bosons  
 624 masses will be generated which is exactly what is needed. In that sense, the best  
 625 choice corresponds to a weak isospin doublet with  $T_3 = -1/2$ ,  $Y_W = 1$  and  $Q = 0$   
 626 which defines a ground state with  $\phi_1 = \phi_2 = \phi_4$  and  $\phi_3 = v$ :

$$\phi_0 \equiv \frac{1}{\sqrt{2}} \begin{pmatrix} 0 \\ v \end{pmatrix}, \quad v^2 \equiv -\frac{\mu^2}{\lambda}. \quad (2.40)$$

627 where the vacuum expectation value  $v$  is fixed by the Fermi coupling  $G_F$  according  
 628 to  $v = (\sqrt{2}G_F)^{1/2} \approx 246$  GeV.

629

630 The G symmetry has been broken and three Nambu-Goldstone bosons will appear.  
 631 The next step is to expand  $\phi$  about the chosen ground state as:

$$\phi(x) = \frac{1}{\sqrt{2}} \exp\left(\frac{i}{v} \sigma_i \theta^i(x)\right) \begin{pmatrix} 0 \\ v + H(x) \end{pmatrix} \approx \frac{1}{\sqrt{2}} \begin{pmatrix} \theta_1(x) + i\theta_2(x) \\ v + H(x) - i\theta_3(x) \end{pmatrix} \quad (2.41)$$

632 to describe fluctuations from the ground state  $\phi_0$ . The fields  $\theta_i(x)$  represent the  
 633 Nambu-Goldstone bosons while  $H(x)$  is known as “higgs field.” The fundamental  
 634 feature of the parametrization used is that the dependence on the  $\theta_i(x)$  fields is  
 635 factored out in a global phase that can be eliminated by taking the physical “unitary  
 636 gauge”  $\theta_i(x) = 0$ . Therefore the expansion about the ground state is given by:

$$\phi(x) \frac{1}{\sqrt{2}} \begin{pmatrix} 0 \\ v + H(x) \end{pmatrix} \quad (2.42)$$

637 which when substituted into  $\mathcal{L}_S$  (eqn. 2.36) results in a Lagrangian containing the now  
 638 massive three gauge bosons  $W^\pm, Z$ , one massless gauge boson (photon) and the new  
 639 Higgs field ( $H$ ). The three degrees of freedom corresponding to the Nambu-Goldstone  
 640 bosons are now integrated into the massive gauge bosons as their longitudinal po-  
 641 larizations which were not available when they were massless particles. The effect  
 642 by which vector boson fields acquire mass after an spontaneous symmetry breaking,  
 643 but without an explicit gauge invariance breaking is known as the “*Higgs mechanism*”.

644

645 The mechanism was proposed by three independent groups: F.Englert and R.Brout  
 646 in August 1964 [29], P.Higgs in October 1964 [30] and G.Guralnik, C.Hagen and  
 647 T.Kibble in November 1964 [31]; however, its importance was not realized until  
 648 S.Glashow [22], A.Salam [23] and S.Weinberg [24], independently, proposed that elec-  
 649 tromagnetic and weak interactions are two manifestations of a more general interac-  
 650 tion called “electroweak interaction” in 1967.

### 651 2.3.3 Masses of the gauge bosons

652 The mass of the gauge bosons is extracted by evaluating the kinetic part of Lagrangian  
 653  $\mathcal{L}_S$  in the ground state (known also as the vacuum expectation value), i.e.,

$$\left| \left( \partial_\mu - ig \frac{\sigma_i}{2} W_\mu^i - i \frac{g'}{2} B_\mu \right) \phi_0 \right|^2 = \left( \frac{1}{2} v g \right)^2 W_\mu^+ W^{-\mu} + \frac{1}{8} v^2 (W_\mu^3, B_\mu) \begin{pmatrix} g^2 & -gg' \\ -gg' & g'^2 \end{pmatrix} \begin{pmatrix} W^{3\mu} \\ B^\mu \end{pmatrix} \quad (2.43)$$

654 comparing with the typical mass term for a charged boson  $M_W^2 W^+ W^-$

$$M_W = \frac{1}{2} v g. \quad (2.44)$$

The second term in the right side of the eqn.2.43 comprises the masses of the neutral

bosons, but it needs to be written in terms of the gauge fields  $Z_\mu$  and  $A_\mu$  in order to be compared to the typical mass terms for neutral bosons, therefore using eqn. 2.28

$$\begin{aligned} \frac{1}{8}v^2[g^2(W_\mu^3)^2 - 2gg'W_\mu^3B^\mu + g'^2B_\mu^2] &= \frac{1}{8}v^2[gW_\mu^3 - g'B_\mu]^2 + 0[g'W_\mu^3 + gB_\mu]^2 \\ &= \frac{1}{8}v^2[\sqrt{g^2 + g'^2}Z_\mu]^2 + 0[\sqrt{g^2 + g'^2}A_\mu]^2 \end{aligned} \quad (2.45)$$

and then

$$M_Z = \frac{1}{2}v\sqrt{g^2 + g'^2}, \quad M_A = 0 \quad (2.46)$$

### 2.3.4 Masses of the fermions

The lepton mass terms can be generated by introducing a gauge invariant Lagrangian term describing the Yukawa coupling between the lepton field and the Higgs field

$$\mathcal{L}_{Yl} = -G_l \left[ (\bar{\nu}_l, \bar{l})_L \begin{pmatrix} \phi^+ \\ \phi^0 \end{pmatrix} l_R + \bar{l}_R (\phi^-, \bar{\phi}^0) \begin{pmatrix} \nu_l \\ l \end{pmatrix}_L \right], \quad l = e, \mu, \tau. \quad (2.47)$$

After the SSB and replacing the usual field expansion about the ground state (eqn.2.40) into  $\mathcal{L}_{Yl}$ , the mass term arises

$$\mathcal{L}_{Yl} = -m_l(\bar{l}_L l_R + \bar{l}_R l_L) - \frac{m_l}{v}(\bar{l}_L l_R + \bar{l}_R l_L)H = -m_l \bar{l} \left( 1 + \frac{H}{v} \right) \quad (2.48)$$

where the additional term represents the lepton-Higgs interaction. The quark masses are generated in a similar way as lepton masses but for the upper member of the

$$m_l = \frac{G_l}{\sqrt{2}}v \quad (2.49)$$

664 quark doublet a different Higgs doublet is needed:

$$\phi_c = -i\sigma_2\phi^* = \begin{pmatrix} -\bar{\phi}^0 \\ \phi^- \end{pmatrix}. \quad (2.50)$$

665 Additionally, given that the quark isospin doublets are not constructed in terms of  
 666 the mass eigenstates but in terms of the flavor eigenstates, as shown in table 2.5, the  
 667 coupling parameters will be related to the CKM matrix elements; thus the quark  
 668 Lagrangian is given by:

$$\mathcal{L}_{Yq} = -G_d^{i,j}(\bar{u}_i, \bar{d}_i)_L \begin{pmatrix} \phi^+ \\ \phi^0 \end{pmatrix} d_{jR} - G_u^{i,j}(\bar{u}_i, \bar{d}_i)_L \begin{pmatrix} -\bar{\phi}^0 \\ \phi^- \end{pmatrix} u_{jR} + h.c. \quad (2.51)$$

669 with  $i,j=1,2,3$ . After SSB and expansion about the ground state, the diagonal form  
 670 of  $\mathcal{L}_{Yq}$  is:

$$\mathcal{L}_{Yq} = -m_d^i \bar{d}_i d_i \left( 1 + \frac{H}{v} \right) - m_u^i \bar{u}_i u_i \left( 1 + \frac{H}{v} \right) \quad (2.52)$$

671 Fermion masses depend on arbitrary couplings  $G_l$  and  $G_{u,d}$  and are not predicted by  
 672 the theory.

### 673 2.3.5 The Higgs field

674 After the characterization of the fermions and gauge bosons as well as their interac-  
 675 tions, it is necessary to characterize the Higgs field itself. The Lagrangian  $\mathcal{L}_S$  in eqn.  
 676 2.3.6 written in terms of the gauge bosons is given by

$$\mathcal{L}_S = \frac{1}{4}\lambda v^4 + \mathcal{L}_H + \mathcal{L}_{HV} \quad (2.53)$$

677

$$\mathcal{L}_H = \frac{1}{2}\partial_\mu H \partial^\mu H - \frac{1}{2}m_H^2 H^2 - \frac{1}{2v}m_H^2 H^3 - \frac{1}{8v^2}m_H^2 H^4 \quad (2.54)$$

678

$$\mathcal{L}_{HV} = m_H^2 W_\mu^+ W^{\mu-} \left( 1 + \frac{2}{v}H + \frac{2}{v^2}H^2 \right) + \frac{1}{2}m_Z^2 Z_\mu Z^\mu \left( 1 + \frac{2}{v}H + \frac{2}{v^2}H^2 \right) \quad (2.55)$$

679 The mass of the Higgs boson is deduced as usual from the mass term in the Lagrangian  
 680 resulting in:

$$m_H = \sqrt{-2\mu^2} = \sqrt{2\lambda}v \quad (2.56)$$

681 however, it is not predicted by the theory either. The experimental efforts to find  
 682 the Higgs boson, carried out by the “Compact Muon Solenoid (CMS)” experiment  
 683 and the “A Toroidal LHC AppartuS (ATLAS)” experiments at the “Large Hadron  
 684 Collider(LHC)”, gave great results by July of 2012 when the discovery of a new  
 685 particle compatible with the Higgs boson predicted by the electroweak theory [32,33]  
 686 was announced. Although at the announcement time there were some reservations  
 687 about calling the new particle the “Higgs boson”, today this name is widely accepted.  
 688 The Higgs mass measurement, reported by both experiments [34], is in table 2.8.

Property	Value
Electric charge	0
Colour charge	0
Spin	0
Weak isospin	-1/2
Weak hypercharge	1
Parity	1
Mass (GeV/c <sup>2</sup> )	125.09±0.21 (stat.)±0.11 (syst.)

**Table 2.8:** Higgs boson properties. Higgs mass is not predicted by the theory and the value here corresponds to the experimental measurement.

689

### 690 2.3.6 Production of Higgs bosons at LHC

691 At LHC, Higgs boson is produced as a result of the collision of two counter-rotating  
 692 protons beams. A detailed description of the LHC machine will be presented in  
 693 chapter 3. “The total cross section” is a parameter that quantifies the number of pp  
 694 collisions that happen when a number of protons are fired at each other. Different  
 695 results can be obtained after a pp collision and for each one the “cross section” is

defined as the number of pp collisions that conclude in that particular result with respect to the number of protons fired at each other.

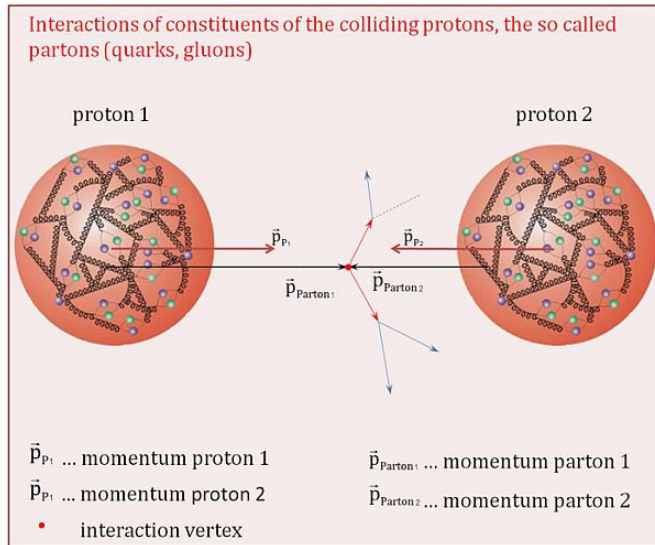


**Figure 2.10:** Proton-proton collision. Protons are composed of 3 valence quarks, a sea of quarks and gluons; therefore in a proton-proton collision, quarks and gluons are those who collide. [35].

697

698 Protons are composed of quarks and these quarks are bound by gluons; however,  
699 what is commonly called the quark content of the proton makes reference to the  
700 valence quarks. A sea of quarks and gluons is also present inside the proton as repre-  
701 sented in figure 2.10. In a proton-proton (pp) collision, the constituents (quarks and  
702 gluons) are those who collide. The pp cross section depends on the momentum of  
703 the colliding particles, reason for which it is needed to know how the momentum is  
704 distributed inside the proton. Quarks and gluons are known as partons and the func-  
705 tions that describe how the proton momentum is distributed among partons inside it  
706 are called “parton distribution functions (PDFs)”; PDFs are determined from experi-  
707 mental data obtained in experiments where the internal structure of hadrons is tested.

708

<sup>709</sup> In addition, in physics, a common approach to study complex systems consists in

710 starting with a simpler version of them, for which a well known description is avail-  
 711 able, and add an additional “perturbation” which represents a small deviation from  
 712 the known behavior. If the perturbation is small enough, the physical quantities as-  
 713 sociated with the perturbed system are expressed as a series of corrections to those  
 714 of the simpler system; therefore, the more terms are considered in the series (the  
 715 higher order in the perturbation series), the more precise is the the description of the  
 716 complex system.

717

718 This thesis explores the Higgs production at LHC; therefore the overview presented  
 719 here will be oriented specifically to the production mechanisms after pp collisions at  
 720 LHC.

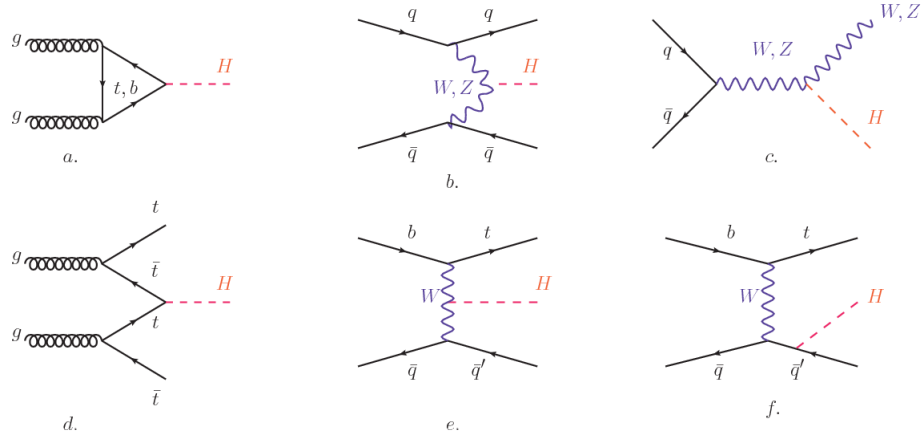


**Figure 2.11:** Main Higgs boson production mechanism Feynman diagrams. a. gluon-gluon fusion, b. vector boson fusion (VBF), c. Higgs-strahlung, d. Associated production with a top or bottom quark pair, e-f. associated production with a single top quark.

721 Figure 2.11 shows the Feynman diagrams for the leading order (first order) Higgs  
 722 production processes at LHC, while the cross section for Higgs production as a func-  
 723 tion of the center of mass-energy ( $\sqrt{s}$ ) for pp collisions is showed in figure 2.12 left.  
 724 The tags NLO (next to leading order), NNLO (next to next to leading order) and  
 725 N3LO (next to next to next to leading order) make reference to the order at which

726 the perturbation series have been considered.

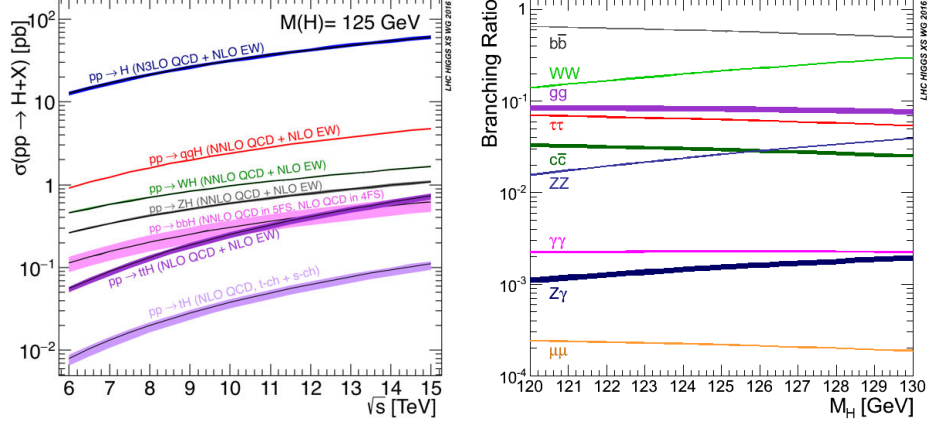


**Figure 2.12:** Higgs boson production cross sections (left) and decay branching ratios (right) for the main mechanisms. The VBF is indicated as  $qqH$  [36].

727 As shown in eqns 2.47, 2.51 and 2.55, the strength of the Higgs-fermion interaction  
 728 is proportional to the fermion mass while the strength of the Higgs-gauge boson  
 729 interaction is proportional to the square of the gauge boson mass, which implies  
 730 that the Higgs production and decay mechanisms are dominated by couplings  $H -$   
 731  $(W, Z, t, b, \tau)$ .

732 The main production mechanism is the gluon fusion (figure 2.11a and  $pp \rightarrow H$  in figure  
 733 2.12) given that gluons carry the highest fraction of momentum of the protons in pp  
 734 colliders. Since the Higgs boson does not couple to gluons, the mechanism proceeds  
 735 through the exchange of a virtual top-quark loop given that for it the coupling is  
 736 the biggest. Note that in this process, the Higgs boson is produced alone, which  
 737 makes this mechanism experimentally clean when combined with the two-photon or  
 738 the four-lepton decay channels (see section 2.3.7).

739 Vector boson fusion (figure 2.11b and  $pp \rightarrow qqH$  in figure 2.12) has the second largest  
 740 production cross section. The scattering of two fermions is mediated by a weak  
 741 gauge boson which later emits a Higgs boson. In the final state, the two fermions

742 tend to be located in a particular region of the detector which is used as a signature  
 743 when analyzing the datasets provided by the experiments. More details about how  
 744 to identify events of interest in an analysis will be given in chapter ??.

745 The next production mechanism is Higgs-strahlung (figure 2.11c and  $pp \rightarrow WH, pp \rightarrow$   
 746  $ZH$  in figure 2.12) where two fermions annihilate to form a weak gauge boson. If the  
 747 initial fermions have enough energy, the emergent boson eventually will emit a Higgs  
 748 boson.

749 The associated production with a top or bottom quark pair and the associated pro-  
 750 duction with a single top quark (figure 2.11d-f and  $pp \rightarrow bbH, pp \rightarrow t\bar{t}H, pp \rightarrow tH$   
 751 in figure 2.12) have a smaller cross section than the main three mechanisms above,  
 752 but they provide a good opportunity to test the Higgs-top coupling. The analysis  
 753 reported in this thesis is developed using these production mechanisms. A detailed  
 754 description of the  $tH$  mechanism will be given in section 2.4.

### 755 2.3.7 Higgs boson decay channels

756 When a particle can decay through several modes, also known as channels, the  
 757 probability of decaying through a given channel is quantified by the “branching ratio  
 758 (BR)” of the decay channel; thus, the BR is defined as the ratio of number of decays  
 759 going through that given channel to the total number of decays. In regard to the  
 760 Higgs boson decay, the BR can be predicted with accuracy once the Higgs mass is  
 761 known [37, 38]. In figure 2.12 right, a plot of the BR as a function of the Higgs mass  
 762 is presented. The largest predicted BR corresponds to the  $b\bar{b}$  pair decay channel (see  
 763 table 2.9).

Decay channel	Branching ratio	Rel. uncertainty
$H \rightarrow b\bar{b}$	$5.84 \times 10^{-1}$	$+3.2\% - 3.3\%$
$H \rightarrow W^+W^-$	$2.14 \times 10^{-1}$	$+4.3\% - 4.2\%$
$H \rightarrow \tau^+\tau^-$	$6.27 \times 10^{-2}$	$+5.7\% - 5.7\%$
$H \rightarrow ZZ$	$2.62 \times 10^{-2}$	$+4.3\% - 4.1\%$
$H \rightarrow \gamma\gamma$	$2.27 \times 10^{-3}$	$+5.0\% - 4.9\%$
$H \rightarrow Z\gamma$	$1.53 \times 10^{-3}$	$+9.0\% - 8.9\%$
$H \rightarrow \mu^+\mu^-$	$2.18 \times 10^{-4}$	$+6.0\% - 5.9\%$

**Table 2.9:** Predicted branching ratios and the relative uncertainty for a SM Higgs boson with  $m_H = 125\text{GeV}/c^2$ . [9]

## 765 2.4 Associated production of a Higgs boson and a 766 single Top quark.

Associated production of Higgs boson has been extensively studied [39–43]. While measurements of the main Higgs production mechanisms rates are sensitive to the strength of the Higgs coupling to W boson or top quark, they are not sensitive to the relative sign between the two couplings. In this thesis, the Higgs boson production mechanism explored is the associated production with a single top quark ( $t\bar{h}$ ) which offers sensitiveness to the relative sign of the Higgs couplings to W boson and to top quark. The description given here is based on the reference [41]

774 A process where two incoming particles interact and produce a final state with two  
775 particles can proceed in three ways also called channels (see, for instance, figure 2.13  
776 omitting the red line). The t-channel represents processes where an intermediate  
777 particle is emitted by one of the incoming particles and absorbed by the other. The  
778 s-channel represents processes where the two incoming particles merge into an inter-  
779 mediate particle which eventually will split into the particles in the final state. The  
780 third channel, u-channel, is similar to the t-channel but the two outgoing particles  
781

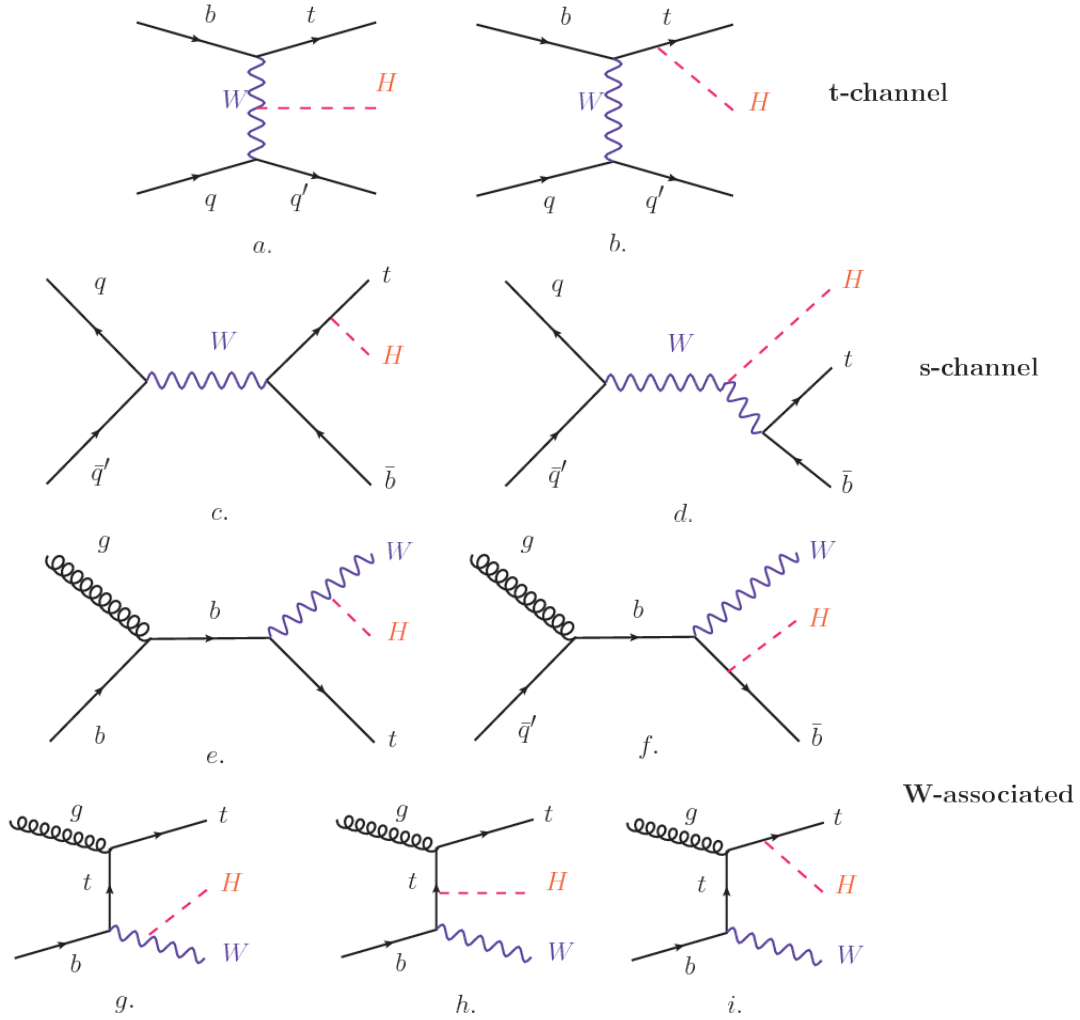


**Figure 2.13:** Associated Higgs boson production mechanism Feynman diagrams. a.,b. t-channel (tHq), c.,d. s-channel (tHb), e-i. W-associated.

782 interchange their roles.

783

784 The  $th$  production, where Higgs boson can be radiated either from the top quark or  
 785 from the  $W$  boson, is represented by the leading order Feynman diagrams in figure  
 786 2.13. The cross section for the  $th$  process is calculated, as usual, summing over  
 787 the contributions from the different feynman diagrams; therefore it depends on the  
 788 interference between the contributions. In the SM, the interference for t-channel (tHq

789 process) and W-associated (tHW process) production is destructive [39] resulting in  
 790 the small cross sections presented in table 2.10.

tH production channel	Cross section (fb)
t-channel ( $pp \rightarrow tHq$ )	$70.79^{+2.99}_{-4.80}$
W-associated ( $pp \rightarrow tHW$ )	$15.61^{+0.83}_{-1.04}$
s-channel( $pp \rightarrow tHb$ )	$2.87^{+0.09}_{-0.08}$

**Table 2.10:** Predicted SM cross sections for  $tH$  production at  $\sqrt{s} = 13$  TeV [44, 45].

791

792 While the s-channel contribution can be neglected, it will be shown that a deviation  
 793 from the SM destructive interference would result in an enhancement of the  $th$  cross  
 794 section compared to that in SM, which could be used to get information about the  
 795 sign of the Higgs-top coupling [41, 42]. In order to describe  $th$  production processes,  
 796 Feynman diagram 2.13b will be considered; there, the W boson is radiated by a  
 797 quark in the proton and eventually it will interact with the b quark. In the high  
 798 energy regime, the effective W approximation [46] allows to describe the process as  
 799 the emmission of an approximately on-shell W and its hard scattering with the b  
 800 quark; i.e.  $Wb \rightarrow th$ . The scattering amplitude for the process is given by

$$\mathcal{A} = \frac{g}{\sqrt{2}} \left[ (\kappa_t - \kappa_V) \frac{m_t \sqrt{s}}{m_W v} A \left( \frac{t}{s}, \varphi; \xi_t, \xi_b \right) + \left( \kappa_V \frac{2m_W s}{v} \frac{1}{t} + (2\kappa_t - \kappa_V) \frac{m_t^2}{m_W v} \right) B \left( \frac{t}{s}, \varphi; \xi_t, \xi_b \right) \right], \quad (2.57)$$

801 where  $\kappa_V \equiv g_{HVV}/g_{HVV}^{SM}$  and  $\kappa_t \equiv g_{Ht}/g_{Ht}^{SM} = y_t/y_t^{SM}$  are scaling factors that quan-  
 802 tify possible deviations of the couplings, Higgs-Vector boson (H-W) and Higgs-top  
 803 (H-t) respectively, from the SM couplings;  $s = (p_W + p_b)^2$ ,  $t = (p_W - p_H)^2$ ,  $\varphi$  is the  
 804 Higgs azimuthal angle around the  $z$  axis taken parallel to the direction of motion of  
 805 the incoming W; A and B are funtions describing the weak interaction in terms of

806 the chiral states of the quarks  $b$  and  $t$ . Terms that vanish in the high energy limit  
 807 have been neglected as well as the Higgs and  $b$  quark masses<sup>8</sup>.

808

809 The scattering amplitude grows with energy like  $\sqrt{s}$  for  $\kappa_V \neq \kappa_t$ , in contrast to  
 810 the SM ( $\kappa_t = \kappa_V = 1$ ), where the first term in 2.57 cancels out and the amplitude  
 811 is constant for large  $s$ ; therefore, a deviation from the SM predictions represents an  
 812 enhancement in the  $tHq$  cross section. In particular, for a SM H-W coupling and a H-t  
 813 coupling of inverted sign with respect to the SM ( $\kappa_V = -\kappa_t = 1$ ) the  $tHq$  cross section  
 814 is enhanced by a factor greater 10 as seen in the figure 2.14 taken from reference [41];  
 815 reference [47] has reported similar enhancement results.

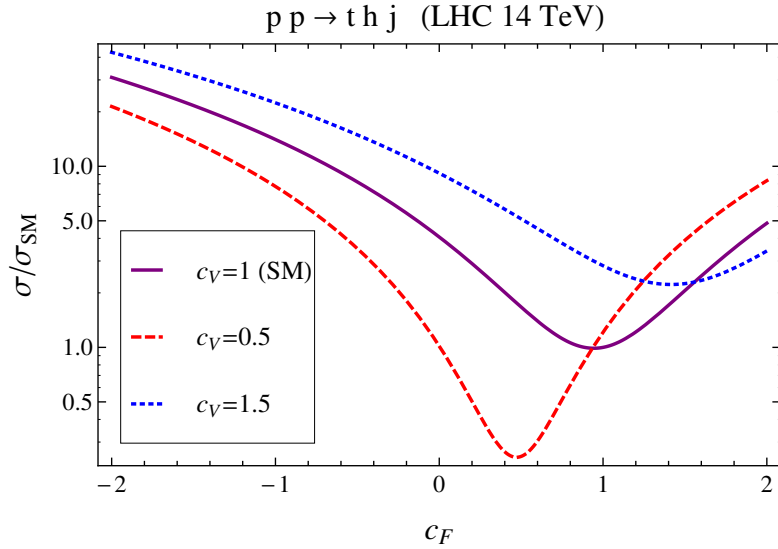


**Figure 2.14:** Cross section for  $tHq$  process as a function of  $\kappa_t$ , normalized to the SM, for three values of  $\kappa_V$ . In the plot  $c_f$  refers to the Higgs-fermion coupling which is dominated by the H-t coupling and represented here by  $\kappa_t$ . Solid, dashed and dotted lines correspond to  $c_V \rightarrow \kappa_V = 1, 0.5, 1.5$  respectively. Note that for the SM ( $\kappa_V = \kappa_t = 1$ ), the destructive effect of the interference is maximal.

816 A similar analysis is valid for the W-associated channel but, in that case, the inter-  
 817 ference is more complicated since there are more than two contributions and an ad-

---

<sup>8</sup> A detailed explanation of the structure and approximations used to derive  $\mathcal{A}$  can be found in reference [41]

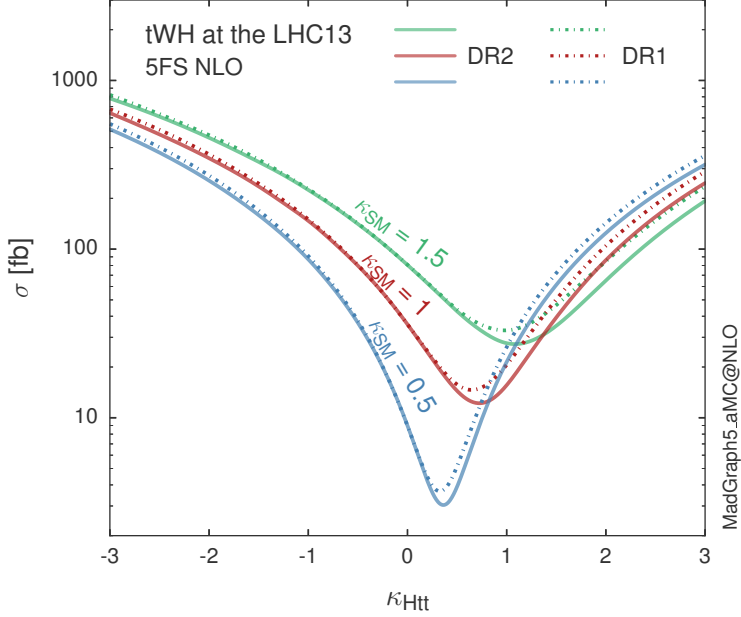


**Figure 2.15:** Cross section for  $tHW$  process as a function of  $\kappa_{Htt}$ , for three values of  $\kappa_{SSM}$  at  $\sqrt{s} = 13$  TeV.  $\kappa_{Htt}^2 = \sigma_{Htt}/\sigma_{Htt}^{SM}$  is a simple rescaling of the SM Higgs interactions.

ditional interference with the production of Higgs boson and a top pair process( $t\bar{t}H$ ).  
 The calculations are made using the so-called Diagram Removal (DR) technique where  
 interfering diagrams are removed (or added) from the calculations in order to evaluate  
 the impact of the removed contributions. DR1 was defined to neglect  $t\bar{t}H$  interference  
 while DR2 was defined to take  $t\bar{t}H$  interference into account [48]. As shown in figure  
 2.15, the  $tHW$  cross section is enhanced from about 15 fb (SM:  $\kappa_{Htt} = 1$ ) to about  
 150 fb ( $\kappa_{Htt} = -1$ ). Differences between curves for DR1 and DR2 help to gauge the  
 impact of the interference with  $t\bar{t}H$ .  
 Results of the calculations of the  $tHq$  and  $tHW$  cross sections at  $\sqrt{s} = 13$  TeV can be  
 found in reference [49] and a summary of the results is presented in table 2.11.

	$\sqrt{s}$ TeV	$\kappa_t = 1$	$\kappa_t = -1$
$\sigma^{LO}(tHq)(fb)$ [41]	8	$\approx 17.4$	$\approx 252.7$
	14	$\approx 80.4$	$\approx 1042$
$\sigma^{NLO}(tHq)(fb)$ [41]	8	$18.28^{+0.42}_{-0.38}$	$233.8^{+4.6}_{-0.0}$
	14	$88.2^{+1.7}_{-0.0}$	$982.8^{+28}_{-0.0}$
$\sigma^{LO}(tHq)(fb)$ [47]	14	$\approx 71.8$	$\approx 893$
$\sigma^{LO}(tHW)(fb)$ [47]	14	$\approx 16.0$	$\approx 139$
$\sigma^{NLO}(tHq)(fb)$ [49]	8	$18.69^{+8.62\%}_{-17.13\%}$	-
	13	$74.25^{+7.48\%}_{-15.35\%}$	$848^{+7.37\%}_{-13.70\%}$
	14	$90.10^{+7.34\%}_{-15.13\%}$	$1011^{+7.24\%}_{-13.39\%}$
$\sigma^{LO}(tHW)(fb)$ [48]	13	$15.77^{+15.91\%}_{-15.76\%}$	-
$\sigma^{NLO}DR1(tHW)(fb)$ [48]	13	$21.72^{+6.52\%}_{-5.24\%}$	$\approx 150$
$\sigma^{NLO}DR2(tHW)(fb)$ [48]	13	$16.28^{+7.34\%}_{-15.13\%}$	$\approx 150$

**Table 2.11:** Predicted enhancement of the  $tHq$  and  $tHW$  cross sections at LHC for  $\kappa_V = 1$  and  $\kappa_t = \pm 1$  at LO and NLO; the cross section enhancement of more than a factor of 10 is due to the flippling in the sign of the H-t coupling with respect to the SM one.

## 829 2.5 The CP-mixing in tH processes

830 In addition to the sensitivity to sign of the H-t coupling,  $tHq$  and  $tHW$  processes have  
 831 been proposed as a tool to investigate the possibility of a H-t coupling that does not  
 832 conserve CP [43, 48, 50]. Current experimental results are consistent with SM H-V  
 833 and H-t couplings; however, negative H-t coupling is not excluded completely [52].

834

835 In this thesis, the sensitivity of  $th$  processes to CP-mixing is also studied in the  
 836 effective field theory framework and based in references [43, 48]; a generic particle  
 837 ( $X_0$ ) of spin-0 and a general CP violating interaction with the top quark, can couple  
 838 to scalar and pseudoscalar fermionic densities. The H-W interaction is assumed to  
 839 be SM-like. The Lagrangian modeling the H-t interaction is given by

$$\mathcal{L}_0^t = -\bar{\psi}_t (c_\alpha \kappa_{Htt} g_{Htt} + i s_\alpha \kappa_{Att} g_{Att} \gamma_5) \psi_t X_0, \quad (2.58)$$

840 where  $\alpha$  is the CP-mixing phase,  $c_\alpha \equiv \cos \alpha$  and  $s_\alpha \equiv \sin \alpha$ ,  $\kappa_{Htt}$  and  $\kappa_{Att}$  are real  
 841 dimensionless rescaling parameters<sup>9</sup>,  $g_{Htt} = g_{Att} = m_t/v = y_t/\sqrt{2}$  and  $v \sim 246$  GeV is  
 842 the Higgs vacuum expectation value. In this parametrization, it is easy to recover  
 843 three special cases

844 • CP-even coupling  $\rightarrow \alpha = 0^\circ$

845 • CP-odd coupling  $\rightarrow \alpha = 90^\circ$

846 • SM coupling  $\rightarrow \alpha = 0^\circ$  and  $\kappa_{Htt} = 1$

847 The loop induced  $X_0$  coupling to gluons can also be described in terms of the  
 848 parametrization above, according to

$$\mathcal{L}_0^g = -\frac{1}{4} \left( c_\alpha \kappa_{Hgg} g_{Hgg} G_{\mu\nu}^a G^{a,\mu\nu} + s_\alpha \kappa_{Agg} g_{Agg} G_{\mu\nu}^a \tilde{G}^{a,\mu\nu} \right) X_0. \quad (2.59)$$

849 where  $g_{Hgg} = -\alpha_s/3\pi v$  and  $g_{Agg} = \alpha_s/2\pi v$ . Under the assumption that the top quark  
 850 dominates the gluon-fusion process at LHC energies,  $\kappa_{Hgg} \rightarrow \kappa_{Htt}$  and  $\kappa_{Agg} \rightarrow \kappa_{Att}$ ,  
 851 so that the ratio between the gluon-gluon fusion cross section for  $X_0$  and for the SM  
 852 Higgs prediction can be written as

$$\frac{\sigma_{NLO}^{gg \rightarrow X_0}}{\sigma_{NLO,SM}^{gg \rightarrow H}} = c_\alpha^2 \kappa_{Htt}^2 + s_\alpha^2 \left( \kappa_{Att} \frac{g_{Agg}}{g_{Hgg}} \right)^2. \quad (2.60)$$

853 If the rescaling parameters are set to

$$\kappa_{Htt} = 1, \quad \kappa_{Att} = \left| \frac{g_{Hgg}}{g_{Agg}} \right| = \frac{2}{3}. \quad (2.61)$$

854 the gluon-fusion SM cross section is reproduced for every value of the CP-mixing  
 855 angle  $\alpha$ ; therefore, by imposing that condition to the Lagrangian density 2.58, the

---

<sup>9</sup> analog to  $\kappa_t$  and  $\kappa_V$

CP-mixing angle is not constrained by current data. Figure 2.16 shows the NLO cross sections for t-channel  $tX_0$ (blue) and  $t\bar{t}X_0$  (red) associated production processes as a function of the CP-mixing angle  $\alpha$ .  $X_0$  is a generic spin-0 particle with top quark CP-violating coupling. Rescaling factors  $\kappa_{Htt}$  and  $\kappa_{Att}$  have been set to reproduce the SM gluon-fusion cross sections.

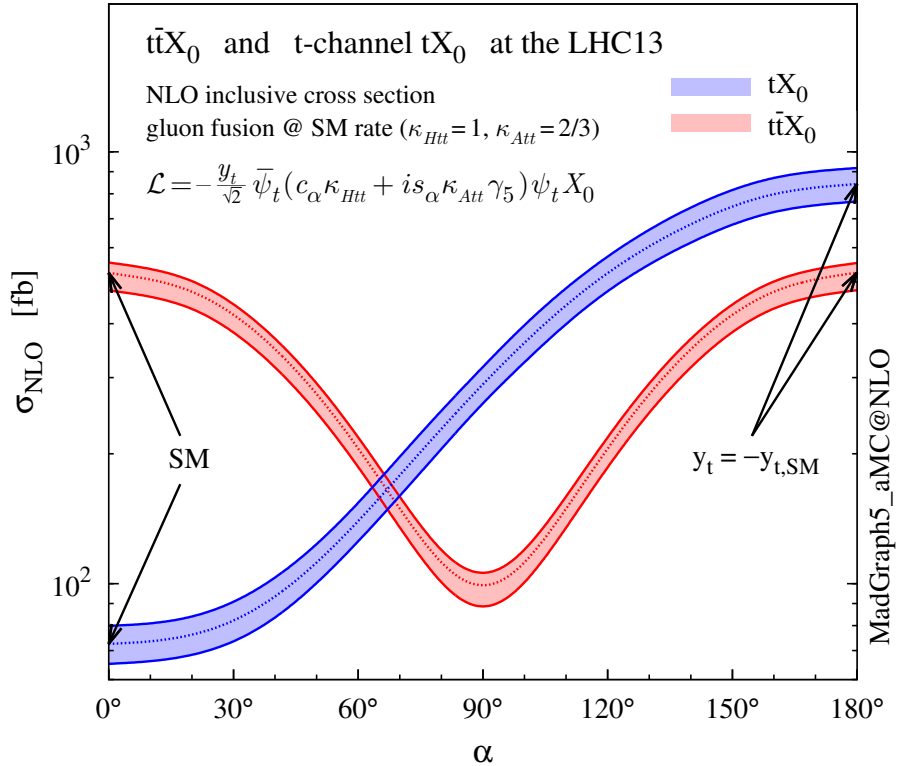


**Figure 2.16:** NLO cross sections for t-channel  $tX_0$ (blue) and  $t\bar{t}X_0$  (red) associated production processes as a function of the CP-mixing angle  $\alpha$ .  $X_0$  is a generic spin-0 particle with top quark CP-violating coupling [43].

It is interesting to notice that the  $tX_0$  cross section is enhanced, by a factor of about 10, when a continuous rotation in the scalar-pseudoscalar plane is applied; this enhancement is similar to the enhancement produced when the H-t coupling is flipped in sign with respect to the SM ( $y_t = -y_{t,SM}$  in the plot), as showed in section 2.4. In contrast, the degeneracy in the  $t\bar{t}X_0$  cross section is still present given that it depends

quadratically on the H-t coupling, but more interesting is to notice that  $t\bar{t}X_0$  cross section is exceeded by  $tX_0$  cross section after  $\alpha \sim 60^\circ$ .

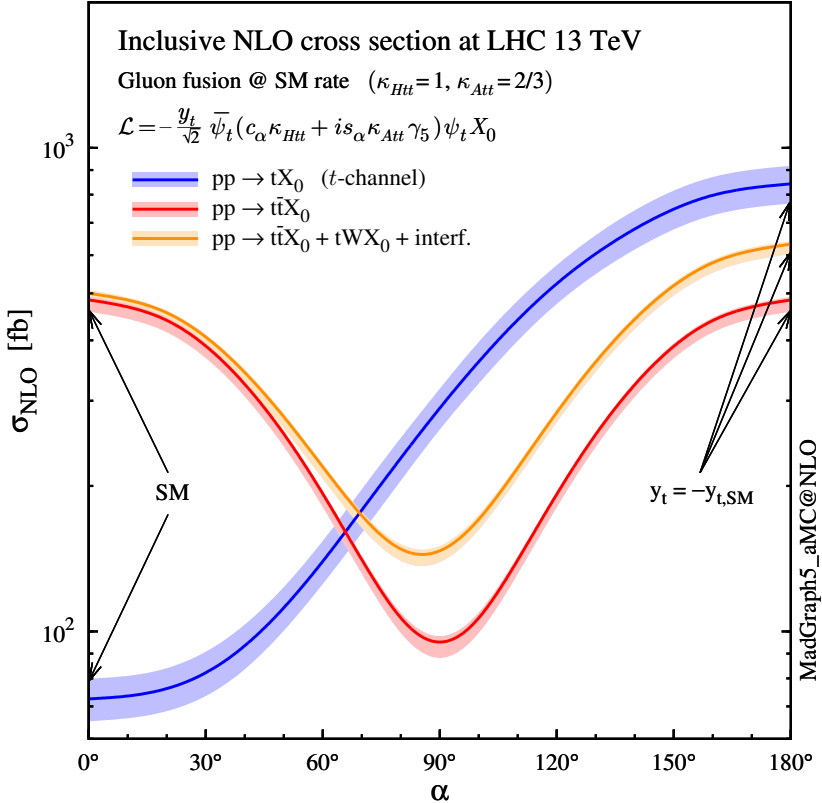


**Figure 2.17:** NLO cross sections for t-channel  $tX_0$ (blue),  $t\bar{t}X_0$  (red) associated production processes and combined  $tWX_0 + t\bar{t}X_0$  (including interference) production as a function of the CP-mixing angle  $\alpha$  [43].

867

868 A similar parametrization can be used to investigate the  $tHW$  process sensitivity to  
 869 CP-violating H-t coupling. As said in 2.4, the interference in the W-associated chan-  
 870 nel is more complicated because there are more than two contributions and also there  
 871 is interference with the  $t\bar{t}H$  production process.

872

873 Figure 2.17 shows the NLO cross sections for t-channel  $tX_0$ (blue),  $t\bar{t}X_0$  (red) asso-  
 874 ciated production and for the combined  $tWX_0 + t\bar{t}X_0 +$  interference (orange) as a  
 875 function of the CP-mixing angle. It is clear that the effect of the interference in the

combined case is the lifting of the degeneracy present in the  $t\bar{t}X_0$  production. The constructive interference enhances the cross section from about 500 fb at SM ( $\alpha = 0$ ) to about 600 fb ( $\alpha = 180^\circ \rightarrow y_t = -y_{t,SM}$ ).

An analysis combining  $tHq$  and  $tHW$  processes will be made in this thesis taking advantage of the sensitivity improvement.

## 2.6 Experimantal status of the anomalous Higg-fermion coupling.

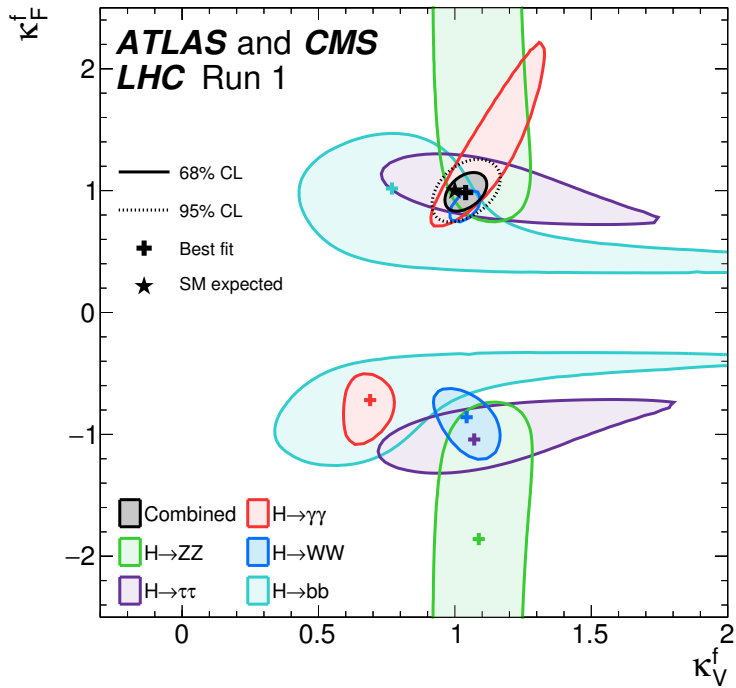


**Figure 2.18:** Combination of the ATLAS and CMS fits for coupling modifiers  $\kappa_t$ - $\kappa_V$ ; also shown the individual decay channels combination and their global combination. No assumptions have been made on the sign of the coupling modifiers [52].

ATLAS and CMS have performed analysis of the anomalous H-f coupling by making likelihood scans for the two coupling modifiers,  $\kappa_t$  and  $\kappa_V$ , under the assumption that

885  $\kappa_Z = \kappa_W = \kappa_V$  and  $\kappa_t = \kappa_\tau = \kappa_b = \kappa_f$ . Figure 2.18 shows the result of the combination  
886 of ATLAS and CMS fits; also the individual decay channels combination and the  
887 global combination results are shown.

888 While all the channels are compatible for positive values of the modifiers, for negative  
889 values of  $\kappa_t$  there is no compatibility. The best fit for individual channels is compatible  
890 with negative values of  $\kappa_t$  except for the  $H \rightarrow bb$  channel which is expected to be the  
891 most sensitive channel; therefore, the best fit for the global fit yields  $\kappa_t \geq 0$ . Thus,  
892 the anomalous H-t coupling cannot be excluded completely.

<sup>893</sup> **Chapter 3**

<sup>894</sup> **The CMS experiment at the LHC**

<sup>895</sup> **3.1 Introduction**

<sup>896</sup> Located on the Swiss-French border, the European Council for Nuclear Research  
<sup>897</sup> (CERN) is the largest scientific organization leading the particle physics research.  
<sup>898</sup> About 13000 people in a broad range of fields including users, students, scientists,  
<sup>899</sup> engineers among others, contribute to the data taking and analysis, with the goal  
<sup>900</sup> of unveiling the secrets of nature and revealing the fundamental structure of the  
<sup>901</sup> universe. CERN is also the home of the Large Hadron Collider (LHC), the largest  
<sup>902</sup> circular particle accelerator around the world, where protons (or heavy ions) traveling  
<sup>903</sup> close to the speed of light, are made to collide. These collisions open a window  
<sup>904</sup> to investigate how particles (and their constituents if they are composite) interact  
<sup>905</sup> with each other, providing clues about the laws of nature. This chapter presents an  
<sup>906</sup> overview of the LHC structure and operation. A detailed description of the CMS  
<sup>907</sup> detector is offered, given that the data used in this thesis have been taken with this  
<sup>908</sup> detector.

## 909 3.2 The LHC

910 With 27 km of circumference, the LHC is currently the largest and most powerful  
 911 circular accelerator in the world. It is installed in the same tunnel where the Large  
 912 Electron-Positron (LEP) collider was located, taking advantage of the existing infras-  
 913 tructure. The LHC is also the larger accelerator in the CERN's accelerator complex  
 914 and is assisted by several successive accelerating stages before the particles are in-  
 915 jected into the LHC ring where they reach their maximum energy (see figure 3.1). 

**Figure 3.1:** CERN accelerator complex. Blue arrows show the path followed by protons along the acceleration process [53].

916 LHC runs  three modes depending on the particles being accelerated

- 917     ● Proton-Proton collisions (pp) for multiple physics experiments.
- 918     ● Lead-Lead collisions (Pb-Pb) for heavy ion experiments.
- 919     ● Proton-Lead collisions (p-Pb) for quark-gluon plasma experiments.

920 In this thesis pp collisions will be considered.

921

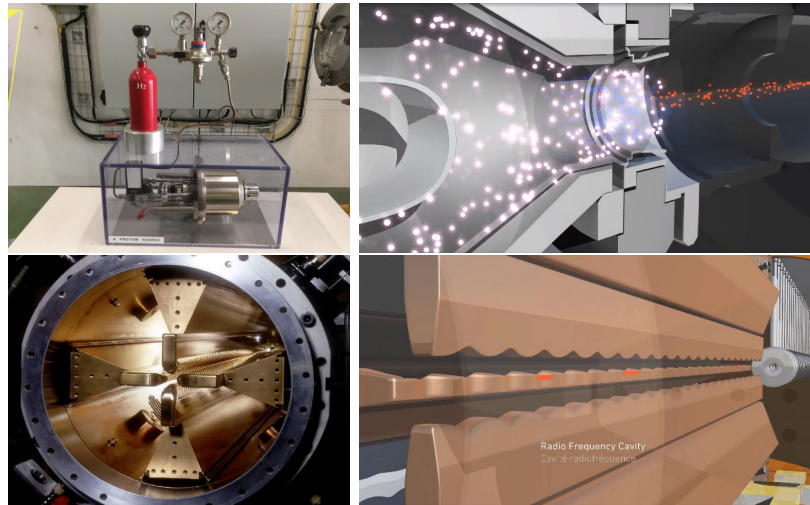


**Figure 3.2:** LHC protons source and the first acceleration stage. Top: the bottle contains hydrogen gas (white dots) which is injected into the metal cylinder to be broken down into electrons(blue dots) and protons(red dots); Bottom: the obtained protons are directed towards the radio frequency quadrupole which perform the first acceleration, focus the beam and create the bunches of protons. [57, 58]

922 Collection of protons starts with hydrogen atoms taken from a bottle, containing hy-  
 923 drogen gas, and injecting them in a metal cylinder; hydrogen atoms are broken down  
 924 into electrons and protons by an intense electric field (see figure3.2 top). The result-  
 925 ing protons leave the metal cylinder towards a radio frequency quadrupole (RFQ)  
 926 that focus the beam, accelerat<sup>T</sup> the protons and creat<sup>O</sup> the packets of protons called  
 927 bunches. In the RFQ, an electric field is generated by a RF wave at a frequency that  
 928 matches the resonance frequency of the cavity where the electrodes are contained.  
 929 The beam of protons traveling on the RFQ axis experie<sup>nc</sup> an alternating electric  
 930 field gradient that generates the focusing forces.

931

932 In order to accelerate the protons, a longitudinal time-varying electric field component  
 933 is added to the system; it is done by giving the electrodes a sinus-like profile as shown  
 934 in figure 3.2 bottom. By matching the speed and phase of the protons with the  
 935 longitudinal electric field the bunching is performed; protons synchronized with the

936 RFQ (synchronous proton) do not feel an accelerating force, but those protons in  
 937 the beam that have more (or less) energy than the synchronous proton (asynchronous  
 938 protons) will feel a decelerating (accelerating) force; therefore, asynchronous protons  
 939 will oscillate around the synchronous ones forming bunches of protons [55]. From the  
 940 RFQ emerge protons with energy 750 keV in bunches of about  $1.15 \times 10^{11}$  protons  
 941 [56].

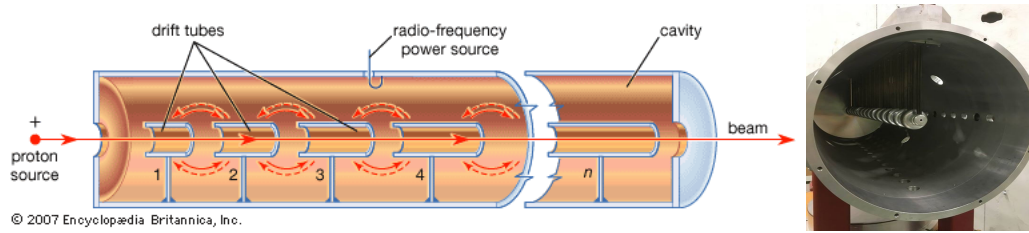


**Figure 3.3:** The LINAC2 accelerating system at CERN. Radio frequency (RF) generated electric fields create acceleration and deceleration zones inside the cavity; deceleration zones are blocked by drift tubes where quadrupole magnets focus the proton beam. [59]

942 Proton bunches coming from the RFQ go to the linear accelerator 2 (LINAC2)  
 943 where they are accelerated to reach 50 MeV energy. In the LINAC2 stage, acceler-  
 944 ation is performed using radio frequency generated electric fields which create zones  
 945 of acceleration and deceleration as shown in figure 3.3. In the decelerations zones,  
 946 the electric field is blocked using drift tubes where protons are free to drift while  
 947 quadrupole magnets focus the beam.

948

949 The beam coming from LINAC2 is injected into the proton synchrotron booster  
 950 (PSB) to reach 1.4 GeV in energy. The next acceleration is provided at the pro-  
 951 ton synchrotron (PS) up to 26 GeV, followed by the injection into the super proton  
 952 synchrotron (SPS) where protons are accelerated to 450 GeV. Finally, protons are  
 953 injected into the LHC where they are accelerated to the target energy of 6.5 TeV.  
 954 PSB, PS, SPS and LHC accelerate protons using the same RF acceleration technic

described before.

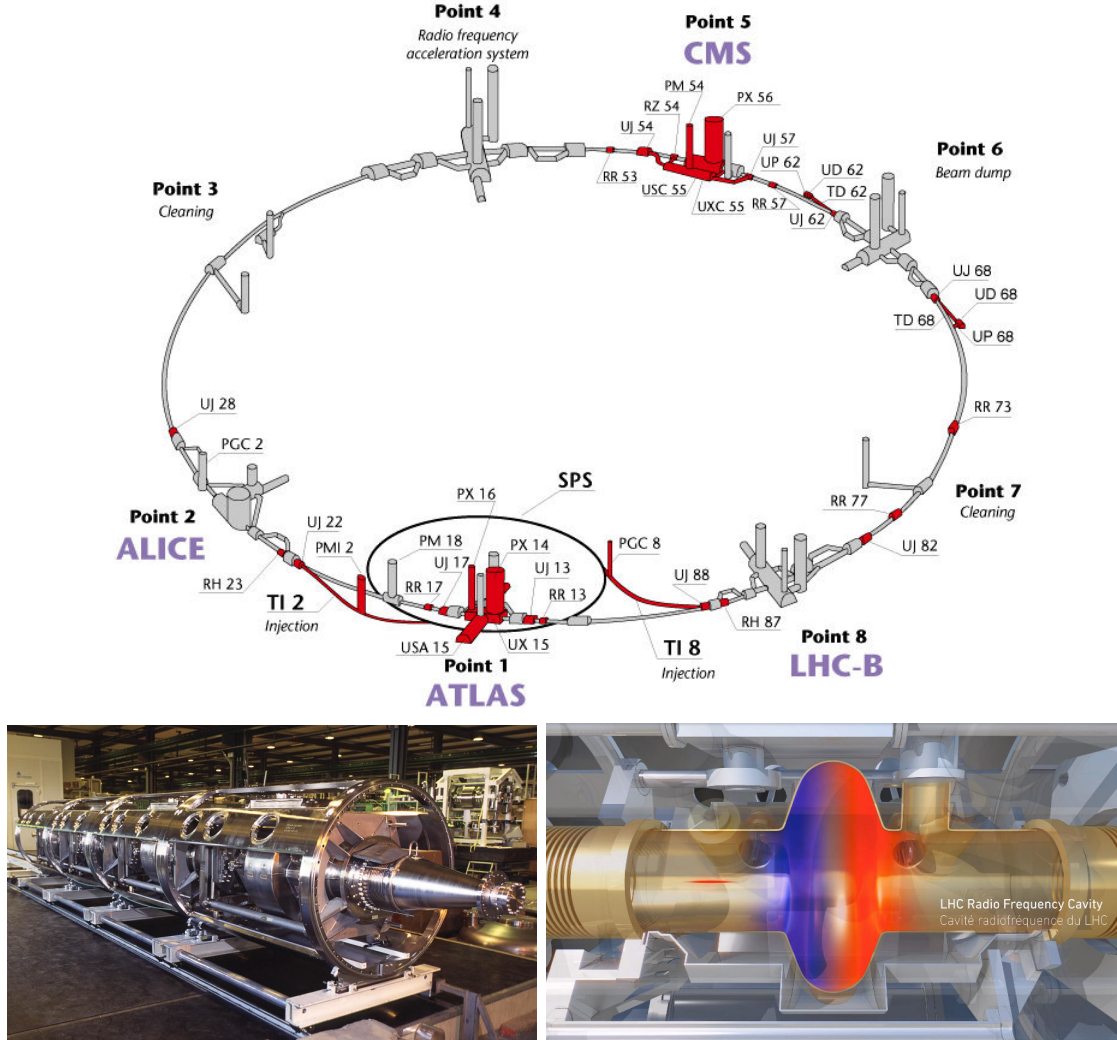


**Figure 3.4:** Top: LHC layout. The red zones indicate the infrastructure additions to the LHC installations, built to accommodate the ATLAS and CMS experiments which exceed the size of the former experiments located there [54]. Bottom: LHC RF cavities. A module accommodates 4 cavities that accelerate protons and preserve the bunch structure of the beam. [58, 60]

LHC has a system of 16 RF cavities located in the so-called point 4, as shown in figure 3.4 top, tuned at a frequency of 400 MHz and the protons are carefully timed so in addition to the acceleration effect the bunch structure of the beam is preserved. Bottom side of figure 3.4 shows a picture of a Rf module composed of 4 RF cavities

960 working in a superconducting state at 4.5 K; also is showed a representation of the  
 961 accelerating electric field that accelerates the protons in the bunch.

962

963 While protons are accelerated in one section of the LHC ring, where the RF cavities  
 964 are located, in the rest of their path they have to be kept in the curved trajectory  
 965 defined by the LHC ring. Technically, LHC is not a perfect circle; RF, injection, beam  
 966 dumping, beam cleaning and sections before and after the experimental points where  
 967 protons collide are all straight sections. In total, there are 8 arcs 2.45 Km long each  
 968 and 8 straight sections 545 m long each. In order to curve the proton's trajectory in  
 969 the arc sections, superconducting dipole magnets are used.

970

971 Inside the LHC ring, there are two proton beams traveling in opposite directions in  
 972 two separated beam pipes; the beam pipes are kept at ultra-high vacuum ( $\sim 10^{-9}$   
 973 Pa) to ensure that there are no particles that interact with the proton beams. The  
 974 superconducting dipole magnets used in LHC are made of a NbTi alloy, capable of  
 975 transporting currents of about 12000 A when cooled at a temperature below 2K using  
 976 liquid helium (see figure 3.5). 

977 Protons in the arc sections of LHC feel a centripetal force exerted by the dipole  
 978 magnets which is perpendicular to the beam trajectory; The magnitude of magnetic  
 979 field needed can be found assuming that protons travel at  $v \approx c$ , using the standard  
 980 values for proton mass and charge and the LHC radius, as

$$F_m = \frac{mv^2}{r} = qBv \quad \rightarrow B = 8.33T \quad (3.1)$$

981 which is about 100000 times the Earth's magnetic field. A representation of the  
 982 magnetic field generated by the dipole magnets is shown in  bottom left side of

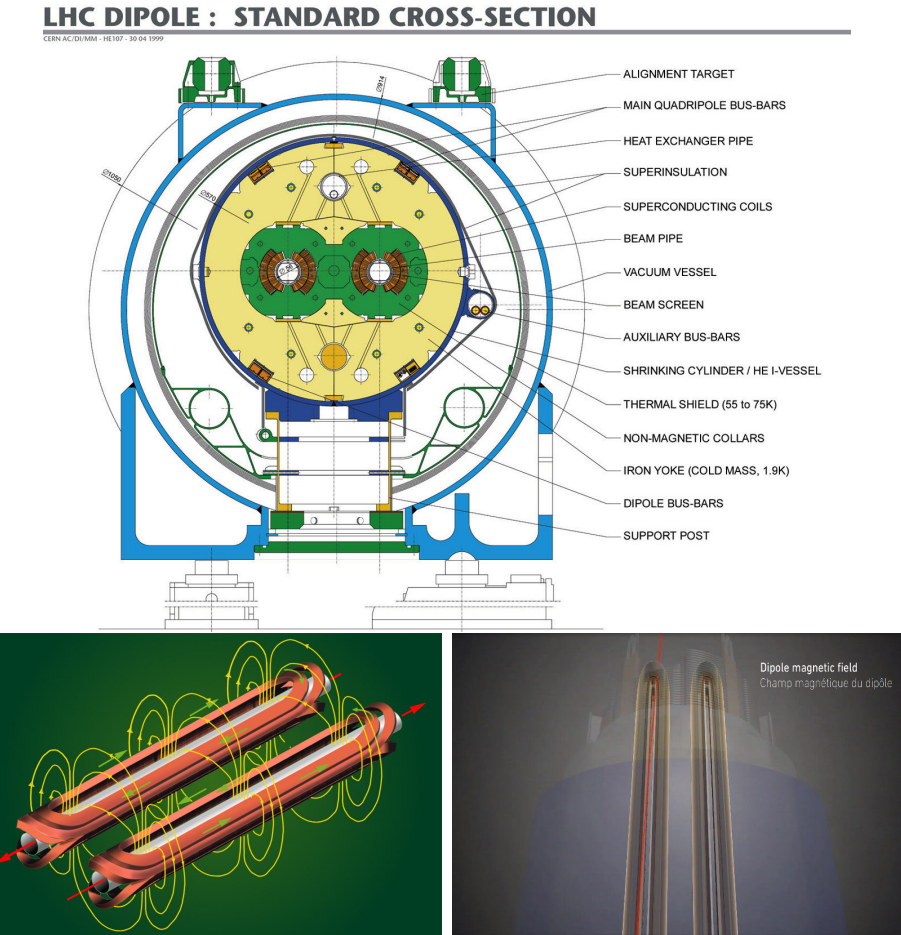


**Figure 3.5:** Top: LHC dipole magnet transversal view; cooling, shielding and mechanical support are indicated. Bottom left: Magnetic field generated by the dipole magnets; note that the direction of the field inside one beam pipe is opposite with respect to the other beam pipe which guarantee that both proton beams are curved in the same direction towards the center of the ring. The effect of the dipole magnetic field on the proton beam is represented in the bottom right side [58, 61, 62].

983 figure 3.5. The bending effect of the magnetic field on the proton beam is shown in 

984 the bottom right side of figure 3.5. Note that the dipole magnets are not curved; the

985 arc section of the LHC ring is composed of straight dipole magnets of about 15 m.

986 In total there are 1232 dipole magnets along the LHC ring.

987 In addition to bending the beam trajectory, the beam has to be focused so it stays

988 inside the beam pipe. The focusing is performed by quadrupole magnets installed

989 in another straight section; in total 858 quadrupole magnets are installed along the  
 990 LHC ring. Other effects like electromagnetic interaction among bunches, interaction  
 991 with electron clouds from the beam pipe, the gravitational force on the protons,  
 992 differences in energy among protons in the same bunch, among others, are corrected  
 993 using sextupole and other magnetic multipoles.

994 The two proton beams inside the LHC ring are made of bunches with a cylindrical  
 995 shape of about 7.5 cm long and about 1 mm in diameter; when bunches are close  
 996 to the collision point (CP), the beam is focused up to a diameter of about 16  $\mu\text{m}$   
 997 in order to maximize the luminosity ( $L$ ) defined as the number of collisions per unit  
 998 area and per second. Luminosity can be calculated using

$$L = fn \frac{N_1 N_2}{4\pi\sigma_x\sigma_y} \quad (3.2)$$

999 where  $f$  is the revolution frequency,  $n$  is the number of bunches per beam,  $N_1$  and  $N_2$   
 1000 are the numbers of protons per bunch,  $\sigma_x$  and  $\sigma_y$  are the gaussian transverse sizes of  
 1001 the bunches. Using

$$f = \frac{v}{2\pi r_{LHC}} \approx \frac{3 \times 10^8 \text{ m/s}}{27 \text{ km}} \approx 11.1 \text{ kHz},$$

$$n = 2808$$

$$N_1 = N_2 = 1.5 \times 10^{11}$$

$$\sigma_x = \sigma_y = 16 \mu\text{m}$$

1002  $L = 1.28 \times 10^{34} \text{ cm}^{-2} \text{ s}^{-1}$  (3.3)

1003 Luminosity is a fundamental aspect for LHC given that the bigger luminosity, the  
 1004 bigger number of collisions, which means that for processes with a very small cross

section the number of expected occurrences is increased and so the chances of being detected. The integrated luminosity collected by the CMS experiment during 2016 is shown in figure 3.6; the data analyzed in this thesis corresponds to an integrated luminosity of  $35.9 \text{ fb}^{-1}$  at  $\sqrt{s} = 13 \text{ TeV}$ .

A way to increase  $L$  is increasing the number of bunches in the beam. Currently, the separation between two consecutive bunches in the beam is 7.5 m which corresponds to a time separation of 25 ns. In the full LHC ring the allowed number of bunches is  $n = 27\text{km}/7.5\text{m} = 3600$ ; however, there are some gaps in the bunch pattern intended for preparing the dumping and injection of the beam, thus, the proton beams are composed of 2808 bunches.

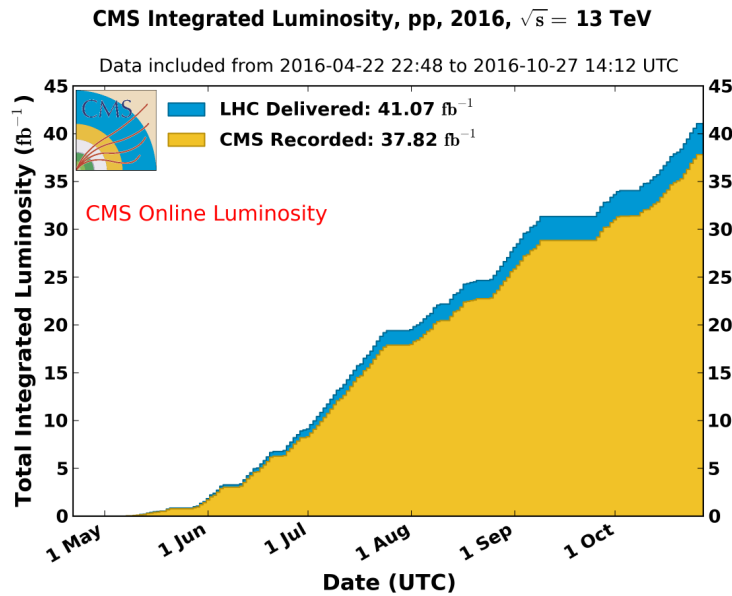


**Figure 3.6:** Integrated luminosity delivered by LHC and recorded by CMS during 2016. The difference between the delivered and the recorded luminosities is due to fails and issues occurred during the data taking in the CMS experiment [63].

Once the proton beams reach the desired energy, they are brought to cross each other producing proton-proton collisions. The bunch crossing happens in precise places where the four LHC experiments are located, as seen in figure 3.7 left. In 2008, the

1018 first set of collisions involved protons with  $\sqrt{s} = 7$  TeV; the energy was increased to  
 1019 8 TeV in 2012 and to 13 TeV in 2015.

1020 CMS and ATLAS experiments, which are multi-purpose experiments, are enabled  
 1021 to explore physics in any of the collision modes. LHCb experiment is optimized  
 1022 to explore bottom quark physics, while ALICE is optimized for heavy ion collisions  
 1023 searches; TOTEM and LHCf are dedicated to forward physics studies; MoEDAL (not  
 1024 indicated in the figure) is intended for monopoles or massive pseudo stable particles  
 1025 searches.

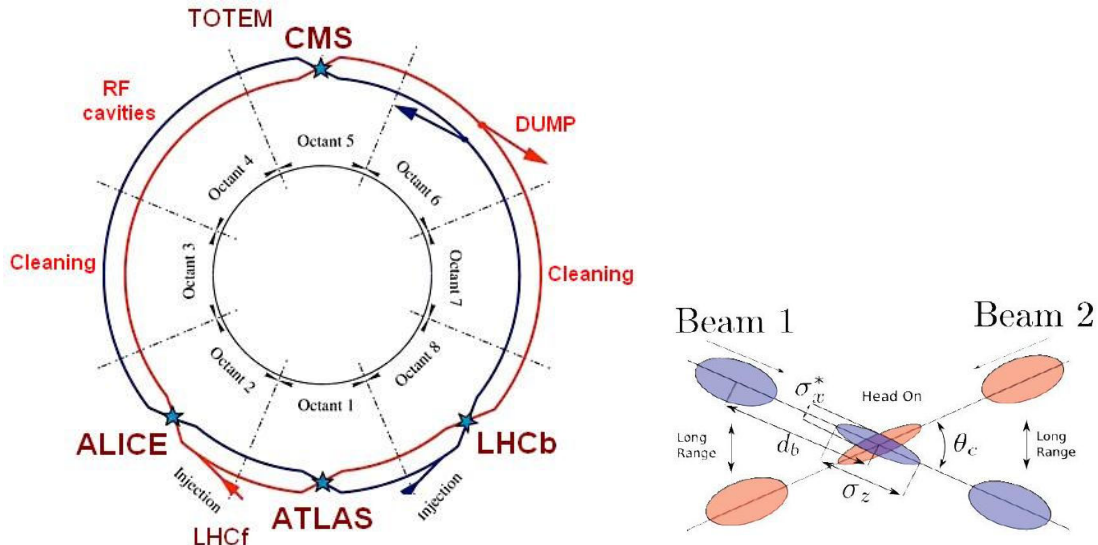


**Figure 3.7:** Left: LHC interaction points. Bunch crossing occurs where the LHC experiments are located [64]. Sections indicated as cleaning are dedicated to collimate the beam in order to protect the LHC ring from collisions with protons in very spreaded bunches. Right: bunch crossing scheme. Since the bunch crossing is not perfectly head-on, the luminosity is reduced in a factor of 17%.

1026 At the CP there are two interesting details that need to be addressed. The first  
 1027 one is that the bunch crossing does not occur head-on but at a small crossing angle  
 1028 (280  $\mu$ rad in CMS and ATLAS) as shown in the right side of figure 3.7, affecting the  
 1029 overlapping between bunches; the consequence is a reduction of about 17% in the  
 1030 luminosity. The second one is the occurrence of multiple pp collisions in the same

1031 bunch crossing; this effect is called pile-up (PU). A fairly simple estimation of the  
 1032 PU follows from estimating the probability of collision between two protons, one from  
 1033 each of the bunches in course of collision; it depends roughly on the ratio of proton  
 1034 size and the cross section of the bunch in the interaction point, i.e.,

$$P(pp\text{-}collision) \sim \frac{d_{proton}^2}{\sigma_x \sigma_y} = \frac{(1fm)^2}{(16\mu m)^2} \sim 4 \times 10^{-21} \quad (3.4)$$

1035 however, there are  $N = 1.15 \times 10^{11}$  protons in a bunch, thus the estimated number of  
 1036 collisions in a bunch crossing is

$$PU = N^2 * P(pp\text{-}collision) \sim 50 \text{ pp-collision per bunch crossing}, \quad (3.5)$$

1037 about 20 of those pp collisions are inelastic. Each collision generates a vertex, but  
 1038 only the most energetic is considered as a primary vertex; the rest are considered as  
 1039 PU vertices. A multiple pp collision event in a bunch crossing at CMS is showed in  
 1040 figure3.8. Unstable particles outgoing from the primary vertex will eventually decay;  
 1041 this decay vertex is known as a secondary vertex.

1042 

1043 Next section presents a description of the CMS detector which it is the detector used  
 1044 to collect the data used in this thesis.

### 1045 3.3 The CMS experiment

1046 CMS is a general-purpose detector designed to conduct research in a wide range  
 1047 of physics from the standard model to new physics like extra dimensions and dark  
 1048 matter. Located at the point 5 in the LHC layout as shown in figure 3.4, CMS is

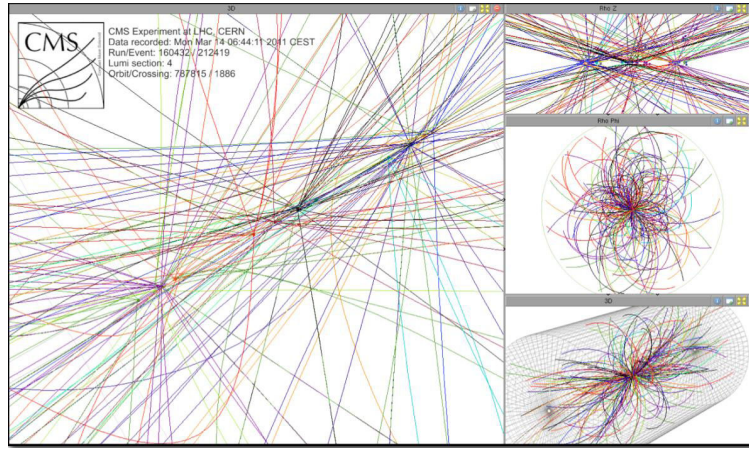


**Figure 3.8:** Multiple pp collision bunch crossing at CMS. Only the most energetic vertex is considered and the jets are cataloged as PU vertices

1049 composed of several detection systems distributed in a cylindrical structure; in total,  
 1050 CMS weights about 12500 tons in a very compact 21.6 m long and 14.6 m diameter  
 1051 cylinder. It was built in 15 separate sections at the ground level and lowered to the  
 1052 cavern individually to be assembled. A complete and detailed description of the CMS  
 1053 detector and its components is given in reference [65] on which this section is based

1054

1055 Figure 3.9 shows the layout of the CMS detector. The design is driven by the require-  
 1056 ments on the identification, momentum resolution and unambiguous charge determi-  
 1057 nation of the muons; therefore, a large bending power is provided by the solenoid  
 1058 magnet made of superconducting cable capable to generate a 3.8 T magnetic field.  
 1059 The detection system is composed of (from the innermost to the outermost)

1060 • Pixel detector.

1061 • Silicon strip tracker.

1062 • Preshower detector.

1063 • Electromagnetic calorimeter.

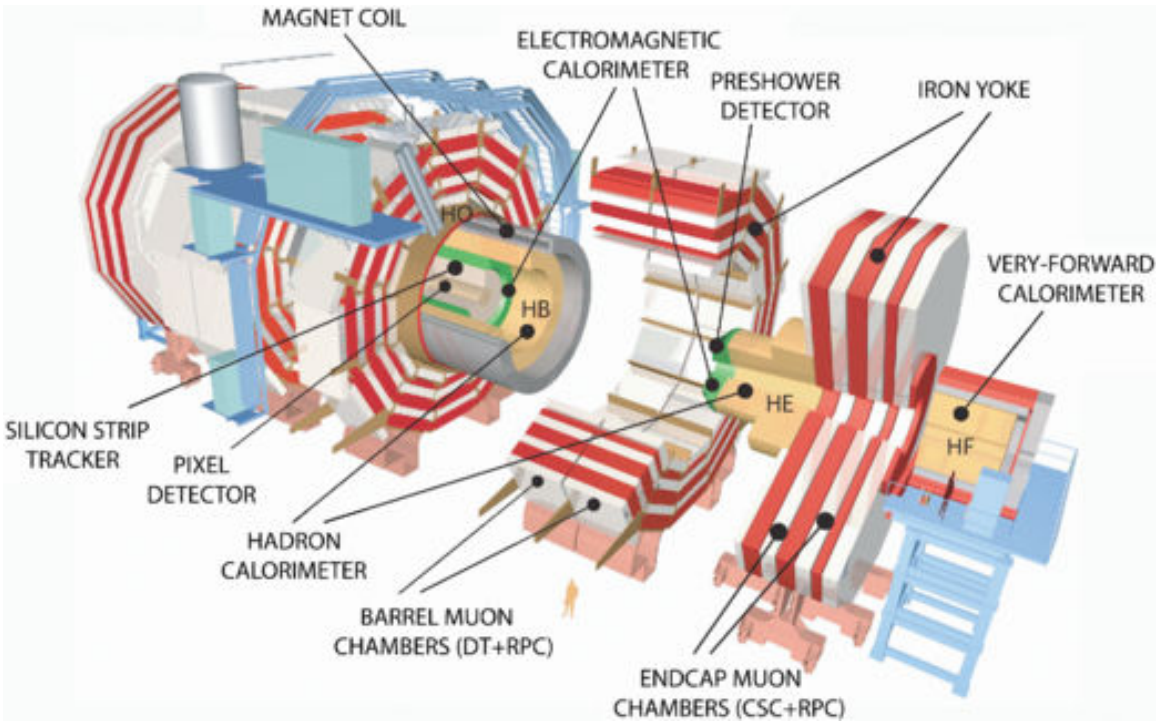


**Figure 3.9:** Layout of the CMS detector. The several subdetectors are indicated. The central region of the detector is referred as the Barrel section while the endcaps are referred as the forward sections. [66].

1064 • Hadronic calorimeter.

1065 • Muon chambers (Barrel and endcap)

1066 The central region of the detector is commonly referred as the barrel section while the  
 1067 endcaps are referred as the forward sections of the detector; thus, each subdetector  
 1068 is composed of a barrel section and a forward section.

### 1069 **3.3.1 Coordinate system**

1070 The coordinate system used by CMS is centered in the geometrical center of the  
 1071 detector which is the same as the CP as shown in figure 3.10. The  $z$ -axis is parallel  
 1072 to the beam direction, while the  $Y$ -axis pointing vertically upward, and the  $X$ -axis  
 1073 pointing radially inward toward the center of the LHC.

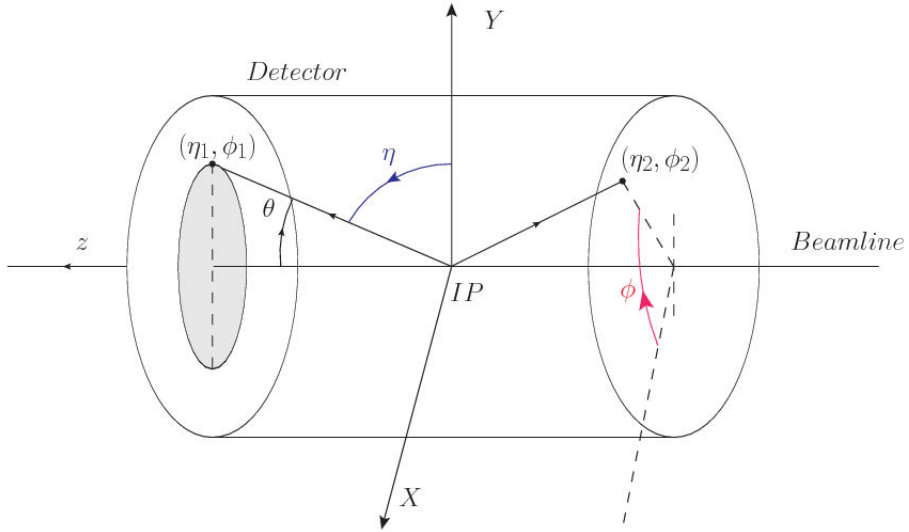


**Figure 3.10:** CMS detector coordinate system.

1074 In addition to the common cartesian and cylindrical coordinate systems, two coordi-  
 1075 nates are of particular utility in particle physics: rapidity( $y$ ) and pseudorapidity( $\eta$ ),  
 1076 defined in connection to the polar angle  $\theta$ , energy and longitudinal momentum com-  
 1077 ponent (momentum along the  $z$ -axis) according to

$$y = \frac{1}{2} \ln \frac{E + p_z}{E - p_z} \quad \eta = -\ln \left( \tan \frac{\theta}{2} \right) \quad (3.6)$$

1078 Rapidity is related to the angle between the  $XY$ -plane and the direction in which the  
 1079 products of a collision are emitted; it has the nice property that the difference between  
 1080 the rapidities of two particles is invariant with respect to Lorentz boosts along the  $z$ -  
 1081 axis. Thus, data analysis becomes more simple when based on rapidity; however, it is  
 1082 not simple to measure the rapidity of highly relativistic particles, as those produced  
 1083 after pp collisions. Under the highly relativistic motion approximation,  $y$  can be  
 1084 rewritten in terms of the polar angle, concluding that rapidity is approximately equal  
 1085 to the pseudorapidity defined above, i.e.  $y \approx \eta$ . Note that  $\eta$  is easier to measure than  $y$   
 1086 given the direct relationship between the former and the polar angle. Angular distance

1087 between two objects in the detector ( $\Delta R$ ) is defined in terms of their coordinates  
 1088  $(\eta_1, \phi_1), (\eta_2, \phi_2)$  as

$$\Delta R = \sqrt{(\Delta\eta)^2 - (\Delta\phi)^2} \quad (3.7)$$

1089 **3.3.2 Pixels detector**

1090 The CMS tracking system is designed to provide a precise measurement of the tra-  
 1091 jectory followed by the charged particles created after the pp collisions  also, the  
 1092 precise reconstruction of the primary and secondary vertices is expected in an envi-  
 1093 ronment where, each 25 ns, the bunch crossing produce about 20 inelastic collisions  
 1094 and about 1000 particles. An increment in the luminosity is ongoing which implies  
 1095 that the PU will increase accordingly.

1096

1097 The pixel detector was replaced during the 2016-2017 year  shut down, due to the  
 1098 increasingly challenging operating conditions like the higher particle flow and more  
 1099 radiation harsh environment  among others. The new one is responding as expected,  
 1100 reinforcing its crucial role in the successful way to fulfill the new LHC physics ob-  
 1101 jectives after the discovery of the Higgs boson. The last chapter of this thesis is  
 1102 dedicated to describe my contribution to the “Forward Pixel Phase 1 up

1103

1104 The current pixel detector is composed of 1856 silicon pixel detector modules orga-  
 1105 nized in four-barrel layers in the central region and three disks in the forward region;  
 1106 it is designed to record efficiently and with high precision, up to  $10\mu\text{m}$  in the  $XY$ -  
 1107 plane and  $20\mu\text{m}$  in the  $z$ -direction, the first four space-points near to the CP region  
 1108 (see figure 3.11 left side) in the range  $|\eta| \leq 2.5$ . The first barrel layer is located at a  
 1109 radius of 30 mm from the beamline, while the fourth layer is located at a radius of

1110 160 mm closer to the strip tracker inner barrel layer (see section 3.3.3) in order to  
 1111 reduce the rate of fake tracks. The high granularity of the detector is represented in  
 1112 its about 123 Mpixels, each of size  $100 \times 150 \mu\text{m}^2$ , which is almost twice the channels  
 1113 of the old detector. The transverse momentum resolution of tracks can be measured  
 1114 with a resolution of 1-2% for muons of  $p_T = 100 \text{ GeV}$ .

1115

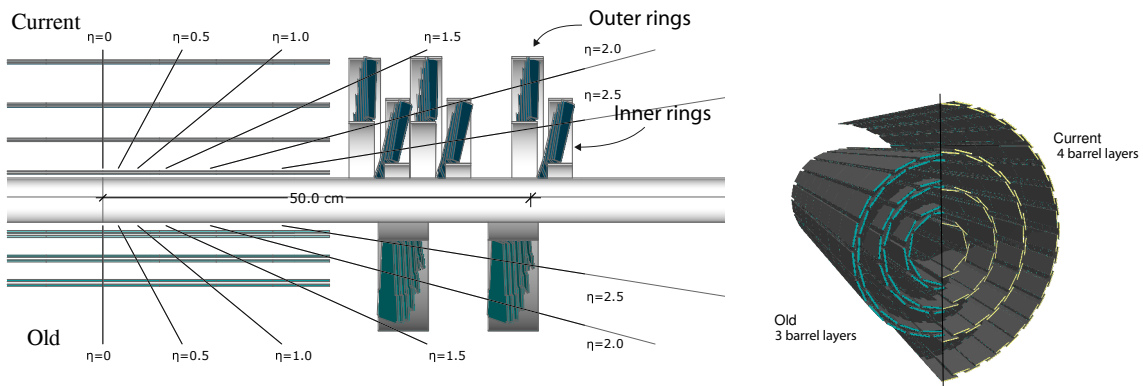


**Figure 3.11:** CMS pixel detector schematic view. Left: layout comparing the layers and disks in the old and current pixel detectors. Right: Transverse-oblique view comparing the pixel barrel layers in the two [68].

1116 Some of the improvements with respect to the previous pixel detector include a higher  
 1117 average tracking efficiency and lower average fake rate as well as higher track impact  
 1118 parameter resolution which is fundamental in order to increase the efficiency in the  
 1119 identification of jets originating from b quarks (b-tagging). A significant source of  
 1120 improvement comes from the overall reduction in the material budget of the detector  
 1121 which results in fewer photon conversions and less multiple scattering from charged  
 1122 particles.

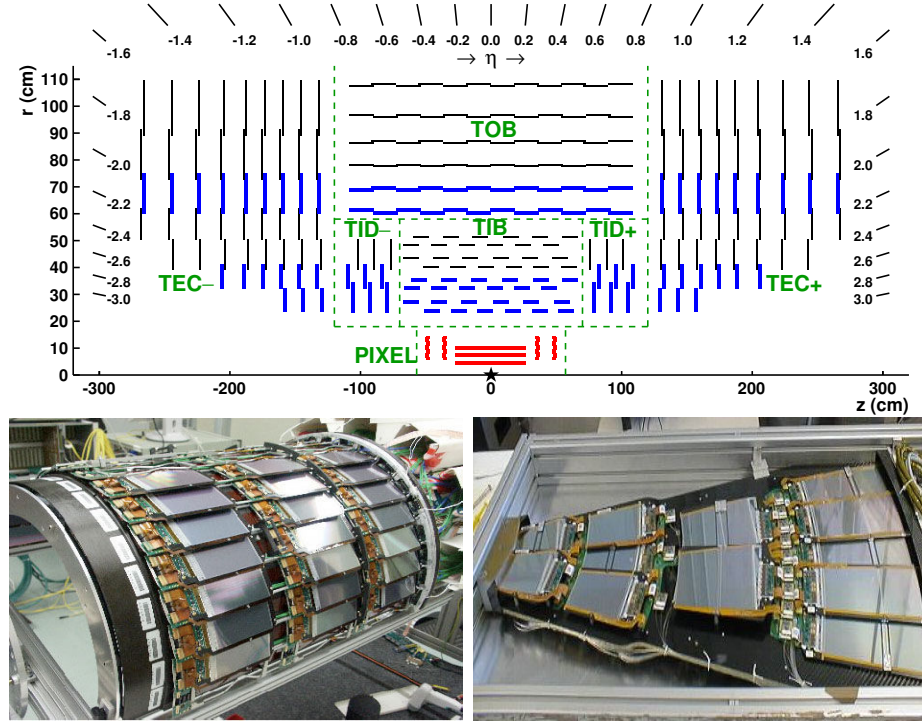


**Figure 3.12:** Top: CMS Si<sup>Si</sup>Strip Tracker (SST) schematic view. The SST is composed of the tracker inner barrel (TIB), the tracker inner disks (TID), the tracker outer barrel (TOB) and the tracker endcaps (TEC). Each part is made of silicon strip modules; the modules in blue represent two modules mounted back-to-back and rotated in the plane of the module by a stereo angle of 120 mrad in order to provide a 3-D reconstruction of the hit positions. Bottom: pictures of the TIB (left) and TEC (right) modules [69–71].

### 1123 3.3.3 Silicon strip tracker

1124 The silicon strip tracker (SST) is the second stage in the CMS tracking system. The  
 1125 top side of figure 3.12 shows a schematic of the SST. The inner tracker region is com-  
 1126 posed of the tracker inner barrel (TIB) and the tracker inner disks (TID) covering the  
 1127 region  $r < 55$  cm and  $|z| < 118$  cm. The TIB is composed of 4 layers while the TID  
 1128 is composed of 3 disks at each end. The silicon sensors in the inner tracker are 320  
 1129  $\mu\text{m}$  thick, providing a resolution of about 13–38  $\mu\text{m}$  in the  $r\phi$  position measurement.

1130

1131 The modules indicated in blue in the schematic view of figure 3.12 are two modules

1132 mounted back-to-back and rotated in the plane of the module by a “stereo” angle of  
 1133 100 mrad; the hits from these two modules, known as “stereo hits”, are combined to  
 1134 provide a measurement of the second coordinate ( $z$  in the barrel and  $r$  on the disks)  
 1135 allowing the reconstruction of hit positions in 3-D.

1136

1137 The outer tracker region is composed of the tracker outer barrel (TOB) and the  
 1138 tracker endcaps (TEC). The 6 layers of the TOB offer coverage in the region  $r > 55$   
 1139 cm and  $|z| < 118$  cm, while the 9 disks of the TEC cover the region  $124 < |z| < 282$   
 1140 cm. The resolution offered by the outer tracker is about 13-38  $\mu\text{m}$  in the  $r\phi$  position  
 1141 measurement. The inner four TEC disks use silicon sensors 320  $\mu\text{m}$  thick; those in  
 1142 the TOB and the outer three TEC disks use silicon sensors of 500  $\mu\text{m}$  thickness. The  
 1143 silicon strips run parallel to the  $z$ -axis and the distance between strips varies from 80  
 1144  $\mu\text{m}$  in the inner TIB layers to 183  $\mu\text{m}$  in the inner TOB layers; in the endcaps the  
 1145 wedge-shaped sensors with radial strips, whose pitch range between 81  $\mu\text{m}$  at small  
 1146 radii and 205  $\mu\text{m}$  at large radii.

1147

1148 The whole SST has 15148 silicon modules, 9.3 million silicon strips and cover a total  
 1149 active area of about 198  $\text{m}^2$

### 1150 3.3.4 Electromagnetic calorimeter

1151 The CMS electromagnetic calorimeter (ECAL) is designed to measure the energy of  
 1152 electrons and photons. It is composed of 75848 lead tungstate crystals which have a  
 1153 short radiation length (0.89 cm) and fast response, since 80% of the light is emitted  
 1154 within 25 ns; however, they are combined with Avalanche photodiodes (APDs) as  
 1155 photodetectors given that crystals themselves have a low light yield ( $30\gamma/\text{MeV}$ ). A

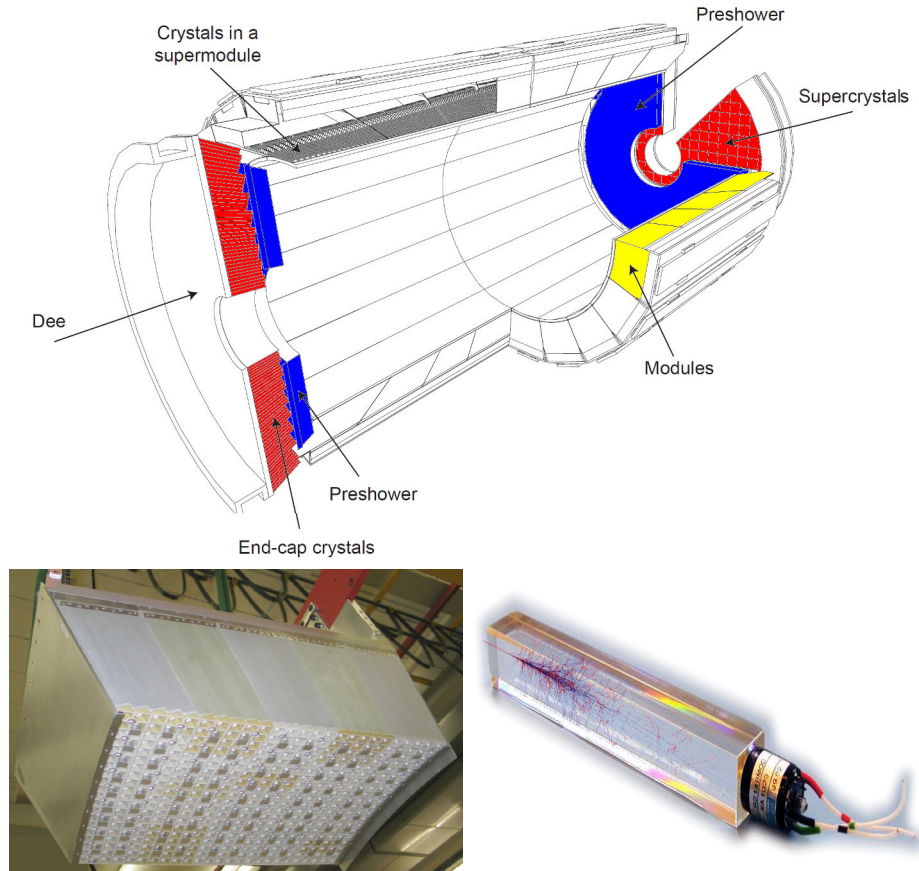


**Figure 3.13:** Top: CMS ECAL schematic view. Bottom: Module equipped with the crystals (left); ECAL crystal(right).

1156 schematic view of the ECAL is shown in figure 3.13.

1157

1158 Energy is measured by absorbing electrons and photons which generates an elec-  
 1159 tromagnetic “shower”, as seen in bottom right picture of the figure 3.13. The ECAL  
 1160 barrel (EB) covers the region  $|\eta| < 1.479$ , using crystals of depth of 23 cm and  $2.2 \times 2.2$   
 1161  $\text{cm}^2$  transverse section.

1162 The ECAL endcap (EE) covers the region  $1.479 < |\eta| < 3.0$  using crystals of depth  
 1163 22 cm and transverse section of  $2.86 \times 2.86 \text{ cm}^2$ ; the photodetectors used are vacuum  
 1164 phototriodes (VPTs). Each EE is divided in two structures called “Dees”.

1165

1166 In front of the EE, it is installed the preshower detector (ES) which covers the region  
 1167  $1.653 < |\eta| < 2.6$ . The ES provides a precise measurement of the position of electro-  
 1168 magnetic showers, which allows to distinguish electrons and photons signals from  $\pi^0$   
 1169 decay signals. The ES is composed of a layer of lead absorber followed by a layer of  
 1170 plastic scintillators

1171 **3.3.5 Hadronic calorimeter**

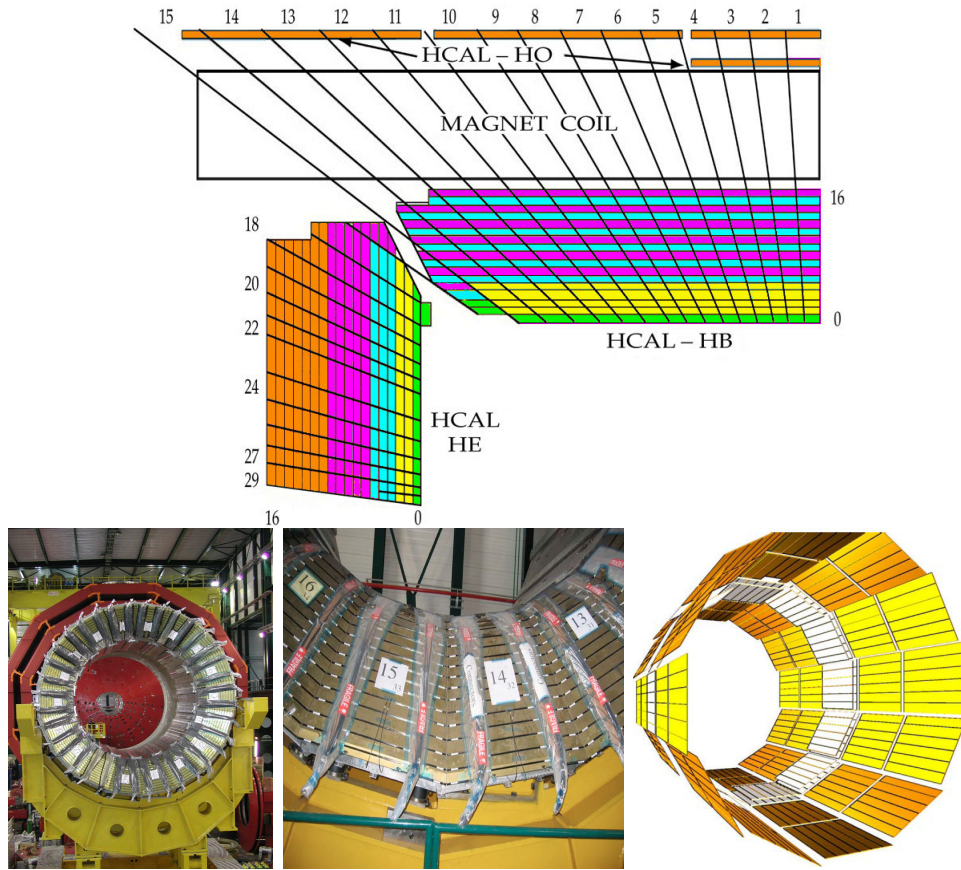


**Figure 3.14:** Top: CMS HCAL schematic view, the colors indicate the layers that are grouped into the same readout channels. Bottom: picture of a section of the HB; the absorber material is the golden region and scintillators are placed in between the absorber material (left and center). Schematic view of the HO (right). [72, 73]

1172 Hadrons are not absorbed by the ECAL but by the hadron calorimeter (HCAL),  
 1173 which is made of a combination of alternating brass absorber and silicon photo-  
 1174 multiplier(SiPM) layers; therefore, particles passing through the scintillator material  
 1175 produce showers, as in the ECAL, as a result of the inelastic scattering of the hadrons  
 1176 with the detector material. Since the particles are not absorbed in the scintillator,  
 1177 their energy is sampled; therefore the total energy is not measured but estimated,  
 1178 which reduce the resolution of the detector. Brass was chosen as the absorber mate-  
 1179 rial due to its short interaction length ( $\lambda_I = 16.42\text{cm}$ ) and its non-magnetivity. Figure  
 1180 3.14 shows a schematic view of the CMS HCAL.

1181

1182 The HCAL is divided into four sections; the Hadron Barrel (HB), the Hadron Outer  
 1183 (HO), the Hadron Endcap (HE) and the Hadron Forward (HF) sections. The HB  
 1184 covers the region  $0 < |\eta| < 1.4$ , while the HE covers the region  $1.3 < |\eta| < 3.0$ . The HF,  
 1185 made of quartz fiber scintillator and steel as absorption material, covers the forward  
 1186 region  $3.0 < |\eta| < 5.2$ . Both the HB and HF are located inside the solenoid. The HO  
 1187 is placed outside the magnet as an additional layer of scintillators with the purpose  
 1188 of measure the energy tails of particles passing through the HB and the magnet  
 1189 (see figure 3.14 top and bottom right). The upgrades made to the HCAL during  
 1190 the technical stop 2016-2017 consisted in the replacement of the photo transducer,  
 1191 improving the efficiency.

### 1192 3.3.6 Superconducting solenoid magnet

1193 The superconducting magnet installed in the CMS detector is designed to provide an  
 1194 intense and highly uniform magnetic field in the central part of the detector. In fact,  
 1195 the tracking system takes advantage of the bending power of the magnetic field to

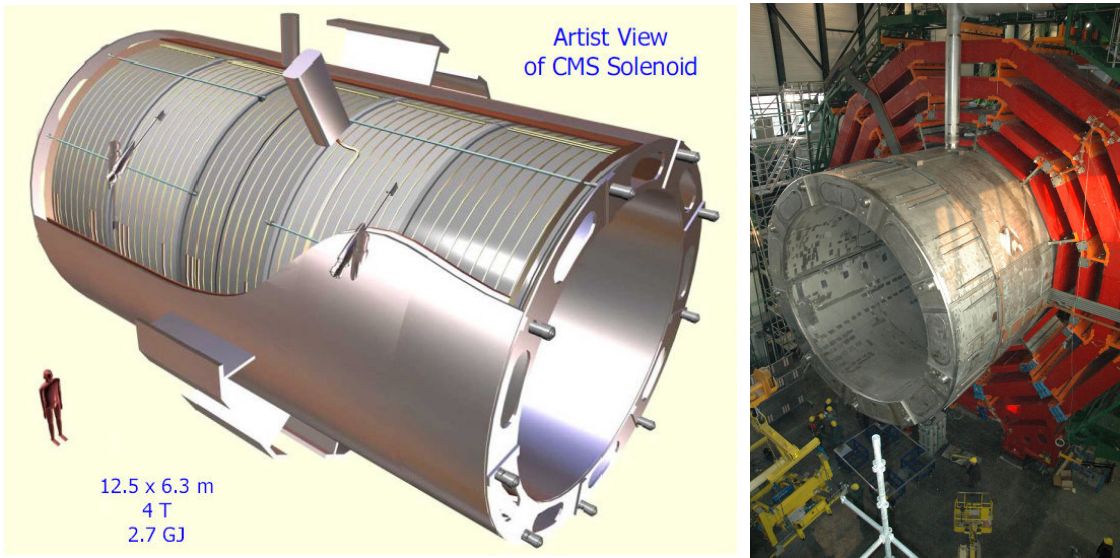


**Figure 3.15:** Artistic representation of the CMS solenoid magnet(left). The magnet is supported on an iron yoke (right) which also serves as the house of the muon detector and as mechanical support for the whole CMS detector [67].

1196 measure with precision the momentum of the particles that traverse it; the unam-  
 1197 biguous determination of the sign for high momentum muons was a driven principle  
 1198 during the design of the magnet. The magnet has a diameter of 6.3 m, a length of  
 1199 12.5 m and a cold mass of 220 t; the generated magnetic field reaches a strength of 3.8T.  
 1200 Since it is made of Ni-Tb superconducting cable it has to operate at a temperature  
 1201 of 4.7 K by using a helium cryogenic system; the current circulating in the cables  
 1202 reaches 18800 A under normal running conditions. The left side of figure 3.15 shows  
 1203 an artistic view of the CMS magnet, while the right side shows a transverse view of  
 1204 the cold mass where the winding structure is visible.  
 1205  
 1206 The yoke (see figure 3.15), composed of 5 barrel wheels and 6 endcap disks made  
 1207 of iron, serves not only as the media for magnetic flux return but also provides the  
 1208 house for the muon detector system and structural stability to the full detector.

1209 **3.3.7 Muon system**

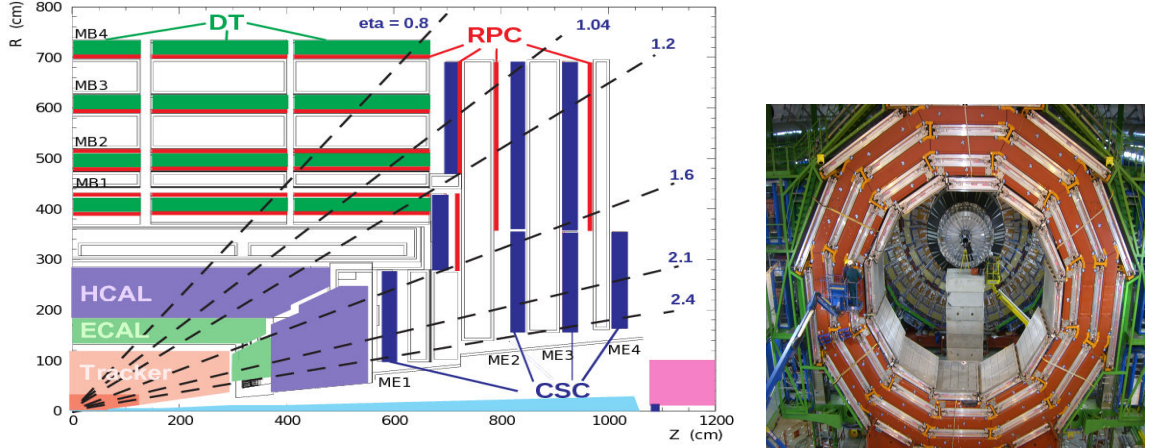


**Figure 3.16:** Left: CMS muon system schematic view; Right: one of the yoke rings with the muon DTs and RPCs installed; in the back it is possible to see the muon endcap [74].

1210 Muons are the only charged particles able to pass through all the CMS detector due to  
 1211 their low ionization energy loss; thus, muons can be separated easily from the high  
 1212 amount of particles produced in a pp collision. Also, muons are expected to be pro-  
 1213 duced in the decay of several new particles; therefore, a good detection of muons was  
 1214 on the leading principles when designing the CMS detector.

1215

1216 The CMS muon detection system is embedded in the return yoke as seen in figure  
 1217 3.16. It is composed of three different detector types The drift tube chambers (DT)  
 1218 are located in the central region  $\eta < 1.2$  arranged in four layers of drift chambers filled  
 1219 with an Ar/CO<sub>2</sub> gas mixture.

1220

1221 The muon endcaps are made of Cathode strip chambers (CSC) covering the region  
 1222  $\eta < 2.4$  and filled with a mixture of Ar/CO<sub>2</sub>/CF<sub>4</sub>. The reason behind using a different  
 1223 detector type lies on the different conditions in the forward region like the high muon  
 1224 rate and high residual magnetic field.

1225

1226 The third type of detector used in the muon system is a set of four disks of resistive  
 1227 plate chambers (RPC) working in avalanche mode. The RPCs provide good spatial  
 1228 and time resolutions. The track of *high* –  $p_T$  muon candidate is built combining  
 1229 information from the tracking system and the signal from up to 6 RPCs and 4 DT  
 1230 chambers.

### 1231 3.3.8 CMS trigger system

1232 Under normal conditions, CMS expects pp collisions every 25 ns between an interaction  
 1233 rate of 40 MHz for which it is not possible to store the recorded data in full. In order  
 1234 to handle this high event rate data, an online event selection, known as triggering, is  
 1235 performed; triggering reduce the event rate to 100 Hz for storage and further offline  
 1236 analysis.

1237

1238 The trigger system starts with a reduction of the event rate to 100 kHz in the so-called  
 1239 “level 1 trigger (L1)”. L1 is based on dedicated programmable hardware like Field  
 1240 Programmable Gate Arrays (FPGAs) and Application Specific Integrated Circuits  
 1241 (ASICs), partly located in the detector itself; another portion is located in the CMS  
 1242 under-ground cavern. Hit patterns information from the muon chambers and the  
 1243 energy deposits in the calorimeter are used to decide if an event is accepted or rejected,  
 1244 according to selection requirements previously defined which reflect the interesting  
 1245 physics processes. Figure 3.17 shows the L1 trigger architecture  
 1246 The second stage in the trigger system is called “high-level trigger (HLT)”; events  
 1247 accepted by L1 are passed to HLT in order to make an initial reconstruction of them.  
 1248 HLT is software based and runs on a dedicated server farm, using selection algo-

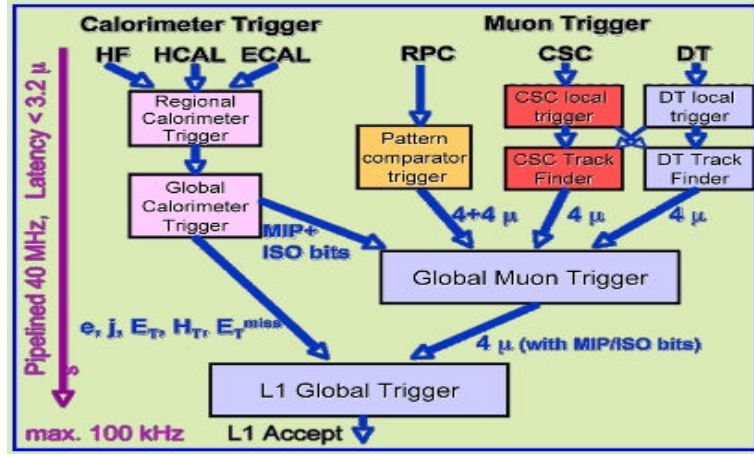


**Figure 3.17:** CMS Level-1 trigger architecture [75].

1249 rithms and high-level object definitions; the event rate at HLT is reduced to 100 Hz.  
 1250 The first HLT stage takes information from the muon detectors and the calorimeters  
 1251 to make the initial object reconstruction; in the next HLT stage, information from  
 1252 the pixel and strip detectors is used to do first fast-tracking and then full tracking  
 1253 online. This initial object reconstruction is used in further steps of the trigger system.

1254

1255 Events and preliminary reconstructed physics objects from HLT are sent to be fully  
 1256 reconstructed at the CERN computing center. Again, the pixel detector information  
 1257 provides high-quality seeds for the track reconstruction algorithm offline, primary ver-  
 1258 tex reconstruction, electron and photon identification, muon reconstruction,  $\tau$  iden-  
 1259 tification, and b-tagging. After full reconstruction, data sets are made available for  
 1260 offline analyses.

1261

1262 During the 2016-2017 technical stop, the L1 system was updated in order to improve  
 1263 the physics object identification by improving the algorithms and accounting for the  
 1264 increasing pile-up scenario.

### 1265 3.3.9 CMS computing

1266 After the data, coming from the experiment, are processed at several levels, they have  
 1267 to be stored and made available for further analysis; in order to cope all the tasks  
 1268 implied in the offline data processing, like transfer, simulation, reconstruction and  
 1269 reprocessing, among others, a big computing power is required. The CMS computing  
 1270 system is based on the distributed architecture concept, where users of the system  
 1271 and physical computer centers are distributed worldwide and interconnected by high-  
 1272 speed networks.

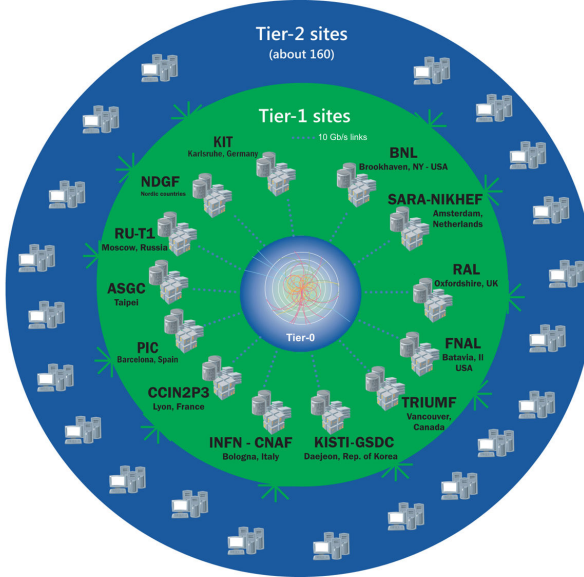


**Figure 3.18:** WLCG structure. The primary computer centers (Tier-0) are located at CERN (data center) and at the Wigner datacenter in Budapest. Tier-1 is composed of 13 centers and Tier-2 is composed of about 160 centers. [76].

1273 The worldwide LHC computing grid (WLCG) is the mechanism used to provide that  
 1274 distributed environment. WLCG is a tiered structure connecting computing centers  
 1275 around the world, which provides the necessary storage and computing facilities. The  
 1276 primary computing centers of the WLCG are located at the CERN and the Wigner  
 1277 datacenter in Budapest and are known as Tier-0 as shown in figure 3.18. The main

1278 responsibilities for each tier level are [76]

1279 • **Tier-0:** initial reconstruction of recorded events and storage of the resulting  
1280 datasets, the distribution of raw data to the Tier-1 centers.

1281 • **Tier-1:** ~~pro<sup>jo</sup>~~ storage capacity, support for the Grid, safe-keeping of a pro-  
1282 portional share of raw and reconstructed data, large-scale reprocessing and safe-  
1283 keeping of corresponding output, generation of simulated events, distribution  
1284 of data to Tier 2s, safe-keeping of a share of simulated data produced at these  
1285 Tier 2s.

1286 • **Tier-2:** ~~st<sup>ro</sup>~~ sufficient data and provide~~e~~ adequate computing power for specific  
1287 analysis tasks, provide~~e~~ analysis requirements and proportional share of simu-  
1288 lated event production and reconstruction.

1289 Aside from the general computing strategy to manage the huge amount of data pro-  
1290 duced by experiments, CMS uses a framework to perform a variety of processing,  
1291 selection and analysis tasks. The central concept of the CMS data model is the  
1292 “Event”; therefore, an event is the unit that contains the information from a single  
1293 bunch crossing as well as any data derived from that information like the recon-  
1294 structed objects, the details under which additional data are derived.

1295

1296 Events are passed as the input to the “physics modules” that obtain information from  
1297 them and create new one; for instance, “event data producers” add new data into the  
1298 events, “analyzers” produce an information summary from an event set, “filters” per-  
1299 form selection and triggering.

1300

1301 CMS uses several event formats with different levels of detail and precision

- 1302     • **Raw format:** events in this format contain the full recorded information from  
1303           the detector as well as trigger decision and other metadata. An extended version  
1304           of raw data is used to store information from the CMS Monte Carlo simulation  
1305           tools. Raw data are stored permanently, occupying about 2MB/event
  - 1306     • **RECO format:** events in this format correspond to raw data that have been  
1307           submitted to reconstruction algorithms like primary and secondary vertex re-  
1308           construction, particle ID, track-finding. RECO events contain physical objects  
1309           and all the information used to reconstruct them; average size is about 0.5  
1310           MB/event.
  - 1311     • **AOD format:** Analysis Object Data (AOD) is the data format used in the  
1312           physics analyses given that it contains the parameters describing the high-level  
1313           physics objects in addition to enough information to allow a kinematic refitting if  
1314           needed. AOD events are filtered versions of the RECO events to which skimming  
1315           or other kind processes have been applied. Requires about 100 kB/event.
  - 1316     • **Non-event data** are data needed to interpret and reconstruct events. Some  
1317           of the non-event data used by CMS contains information about the detector  
1318           contraction and condition data like calibrations, alignment, and detector status.
- 1319    Figure 3.19 shows the data flow scheme between CMS detector and hardware tiers.

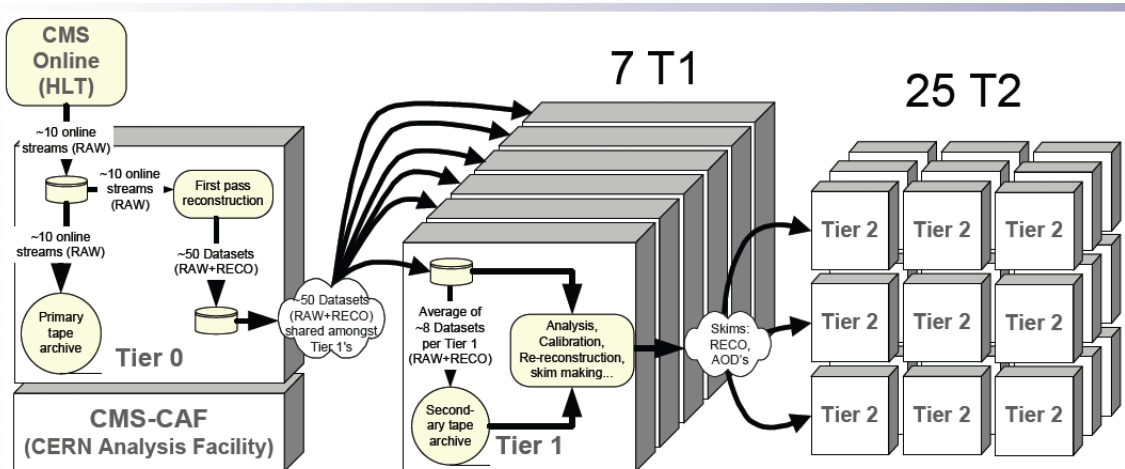


**Figure 3.19:** Data flow from CMS detector through hardware Tiers.



<sub>1320</sub> **Chapter 4**

<sub>1321</sub> **Event generation, simulation and  
<sub>1322</sub> reconstruction**

<sub>1323</sub> **4.1 Introduction**

<sub>1324</sub> **4.2 event generation**

<sub>1325</sub> **4.3 Hard scattering**

<sub>1326</sub> **4.4 parton shower**

<sub>1327</sub> **4.5 hadronization and decays**

<sub>1328</sub> **4.6 underlying events and pileup**

<sub>1329</sub> **4.7 MC - MadEvent, MadGraph and**

<sub>1330</sub> **madgraphNLO, powheg, pythia, tauola**

<sub>1331</sub> **4.8 detector simulation**

# 1343 References

- 1344 [1] J. Schwinger. "Quantum Electrodynamics. I. A Covariant Formulation". Physical Review. 74 (10): 1439-61, (1948).
- 1345
- 1346 [2] R. P. Feynman. "Space-Time Approach to Quantum Electrodynamics". Physical Review. 76 (6): 769-89, (1949).
- 1347
- 1348 [3] S. Tomonaga. "On a Relativistically Invariant Formulation of the Quantum Theory of Wave Fields". Progress of Theoretical Physics. 1 (2): 27-42, (1946).
- 1349
- 1350 [4] D.J. Griffiths, "Introduction to electrodynamics". 4th ed. Pearson, (2013).
- 1351 [5] F. Mandl, G. Shaw. "Quantum field theory." Chichester: Wiley (2009).
- 1352 [6] F. Halzen, and A.D. Martin, "Quarks and leptons: An introductory course in modern particle physics". New York: Wiley, (1984) .
- 1353
- 1354 [7] File: Standard\_Model\_of\_Elementary\_Particle\_dark.svg. (2017, June 12) Wikimedia Commons, the free media repository. Retrieved November 27, 2017 from <https://www.collegiate-advanced-electricity.com/single-post/2017/04/10/The-Standard-Model-of-Particle-Physics>.
- 1355
- 1356
- 1357
- 1358 [8] E. Noether, "Invariante Variationsprobleme", Nachrichten von der Gesellschaft der Wissenschaften zu Göttingen, mathematisch-physikalische Klasse, vol. 1918, pp. 235-257, (1918).
- 1359
- 1360

- 1361 [9] C. Patrignani et al. (Particle Data Group), Chin. Phys. C, 40, 100001 (2016)  
1362 and 2017 update.
- 1363 [10] M. Goldhaber, L. Grodzins, A.W. Sunyar “Helicity of Neutrinos”, Phys. Rev.  
1364 109, 1015 (1958).
- 1365 [11] Palanque-Delabrouille N et al. “Neutrino masses and cosmology with Lyman-  
1366 alpha forest power spectrum”, JCAP 11 011 (2015).
- 1367 [12] M. Gell-Mann. “A Schematic Model of Baryons and Mesons”. Physics Letters.  
1368 8 (3): 214-215 (1964).
- 1369 [13] G. Zweig. “An SU(3) Model for Strong Interaction Symmetry and its Breaking”  
1370 (PDF). CERN Report No.8182/TH.401 (1964).
- 1371 [14] G. Zweig. “An SU(3) Model for Strong Interaction Symmetry and its Breaking:  
1372 II” (PDF). CERN Report No.8419/TH.412(1964).
- 1373 [15] M. Gell-Mann. “The Interpretation of the New Particles as Displaced Charged  
1374 Multiplets”. Il Nuovo Cimento 4: 848. (1956).
- 1375 [16] T. Nakano, K, Nishijima. “Charge Independence for V-particles”. Progress of  
1376 Theoretical Physics 10 (5): 581-582. (1953).
- 1377 [17] N. Cabibbo, “Unitary symmetry and leptonic decays” Physical Review Letters,  
1378 vol. 10, no. 12, p. 531, (1963).
- 1379 [18] M.Kobayashi, T.Maskawa, “CP-violation in the renormalizable theory of weak  
1380 interaction,” Progress of Theoretical Physics, vol. 49, no. 2, pp. 652-657, (1973).
- 1381 [19] File: Weak Decay (flipped).svg. (2017, June 12). Wikimedia Com-  
1382 mons, the free media repository. Retrieved November 27, 2017 from

- 1383 https://commons.wikimedia.org/w/index.php?title=File:Weak\_Decay\_(flipped)  
1384 .svg&oldid=247498592.
- 1385 [20] Georgia Tech University. Coupling Constants for the Fundamental  
1386 Forces(2005). Retrieved January 10, 2018, from http://hyperphysics.phy-  
1387 astr.gsu.edu/hbase/Forces/couple.html#c2
- 1388 [21] M. Strassler. (May 31, 2013).The Strengths of the Known Forces. Retrieved Jan-  
1389 uary 10, 2018, from https://profmattstrassler.com/articles-and-posts/particle-  
1390 physics-basics/the-known-forces-of-nature/the-strength-of-the-known-forces/
- 1391 [22] S.L. Glashow. “Partial symmetries of weak interactions”, Nucl. Phys. 22 579-  
1392 588, (1961).
- 1393 [23] A. Salam, J.C. Ward. “Electromagnetic and weak interactions”, Physics Letters  
1394 13 168-171, (1964).
- 1395 [24] S. Weinberg, “A model of leptons”, Physical Review Letters, vol. 19, no. 21, p.  
1396 1264, (1967).
- 1397 [25] M. Peskin, D. Schroeder, “An introduction to quantum field theory”. Perseus  
1398 Books Publishing L.L.C., (1995).
- 1399 [26] A. Pich. “The Standard Model of Electroweak Interactions”  
1400 https://arxiv.org/abs/1201.0537
- 1401 [27] F.Bellaiche. (2012, 2 September). “What’s this Higgs boson anyway?”. Retrieved  
1402 from: https://www.quantum-bits.org/?p=233
- 1403 [28] M. Endres et al. Nature 487, 454-458 (2012) doi:10.1038/nature11255

- 1404 [29] F. Englert, R. Brout. “Broken Symmetry and the Mass of Gauge  
 1405 Vector Mesons”. Physical Review Letters. 13 (9): 321-23.(1964)  
 1406 doi:10.1103/PhysRevLett.13.321
- 1407 [30] P.Higgs. “Broken Symmetries and the Masses of Gauge Bosons”. Physical Re-  
 1408 view Letters. 13 (16): 508-509,(1964). doi:10.1103/PhysRevLett.13.508.
- 1409 [31] G.Guralnik, C.R. Hagen and T.W.B. Kibble. “Global Conservation Laws  
 1410 and Massless Particles”. Physical Review Letters. 13 (20): 585-587, (1964).  
 1411 doi:10.1103/PhysRevLett.13.585.
- 1412 [32] CMS collaboration. “Observation of a new boson at a mass of 125 GeV with  
 1413 the CMS experiment at the LHC”. Physics Letters B. 716 (1): 30-61 (2012).  
 1414 arXiv:1207.7235. doi:10.1016/j.physletb.2012.08.021
- 1415 [33] ATLAS collaboration. “Observation of a New Particle in the Search for the Stan-  
 1416 dard Model Higgs Boson with the ATLAS Detector at the LHC”. Physics Letters  
 1417 B. 716 (1): 1-29 (2012). arXiv:1207.7214. doi:10.1016/j.physletb.2012.08.020.
- 1418 [34] ATLAS collaboration; CMS collaboration (26 March 2015). “Combined Mea-  
 1419 surement of the Higgs Boson Mass in pp Collisions at  $\sqrt{s}=7$  and 8 TeV with  
 1420 the ATLAS and CMS Experiments”. Physical Review Letters. 114 (19): 191803.  
 1421 arXiv:1503.07589. doi:10.1103/PhysRevLett.114.191803.
- 1422 [35] LHC InternationalMasterclasses“When protons collide”. Retrieved from  
 1423 [http://atlas.physicsmasterclasses.org/en/zpath\\_protoncollisions.htm](http://atlas.physicsmasterclasses.org/en/zpath_protoncollisions.htm)
- 1424 [36] CMS Collaboration, “SM Higgs Branching Ratios and To-  
 1425 tal Decay Widths (up-date in CERN Report4 2016)”).

- 1426 https://twiki.cern.ch/twiki/bin/view/LHCPhysics/CERNYellowReportPageBR  
 1427 , last accessed on 17.12.2017.
- 1428 [37] R.Grant V. “Determination of Higgs branching ratios in  $H \rightarrow W^+W^- \rightarrow l\nu jj$  and  $H \rightarrow ZZ \rightarrow l^+l^-jj$  channels”. Physics Department, Uni-  
 1429 versity of Tennessee (Dated: October 31, 2012). Retrieved from  
 1430 http://aesop.phys.utk.edu/ph611/2012/projects/Riley.pdf
- 1431
- 1432 [38] LHC Higgs Cross Section Working Group, Denner, A., Heinemeyer, S. et al.  
 1433 “Standard model Higgs-boson branching ratios with uncertainties”. Eur. Phys.  
 1434 J. C (2011) 71: 1753. <https://doi.org/10.1140/epjc/s10052-011-1753-8>
- 1435 [39] F. Maltoni, K. Paul, T. Stelzer, and S. Willenbrock, “Associated production  
 1436 of Higgs and single top at hadron colliders”, Phys.Rev. D64 (2001) 094023,  
 1437 [hep-ph/0106293].
- 1438 [40] S. Biswas, E. Gabrielli, F. Margaroli, and B. Mele, “Direct constraints on the  
 1439 top-Higgs coupling from the 8 TeV LHC data,” Journal of High Energy Physics,  
 1440 vol. 07, p. 073, (2013).
- 1441 [41] M. Farina, C. Grojean, F. Maltoni, E. Salvioni, and A. Thamm, “Lifting de-  
 1442 generacies in Higgs couplings using single top production in association with a  
 1443 Higgs boson,” Journal of High Energy Physics, vol. 05, p. 022, (2013).
- 1444 [42] T.M. Tait and C.-P. Yuan, “Single top quark production as a window to physics  
 1445 beyond the standard model”, Phys. Rev. D 63 (2000) 014018 [hep-ph/0007298].
- 1446 [43] F. Demartin, F. Maltoni, K. Mawatari, and M. Zaro, “Higgs production in  
 1447 association with a single top quark at the LHC,” European Physical Journal C,  
 1448 vol. 75, p. 267, (2015).

- 1449 [44] CMS Collaboration, “Modelling of the single top-quark pro-  
 1450 duction in association with the Higgs boson at 13 TeV.”  
 1451 <https://twiki.cern.ch/twiki/bin/viewauth/CMS/SingleTopHiggsGeneration13TeV>,  
 1452 last accessed on 16.01.2018.
- 1453 [45] CMS Collaboration, “SM Higgs production cross sections at  $\sqrt{s} = 13$  TeV.”  
 1454 <https://twiki.cern.ch/twiki/bin/view/LHCPhysics/CERNYellowReportPageAt13TeV>, last  
 1455 accessed on 16.01.2018.
- 1456 [46] S. Dawson, The effective W approximation, Nucl. Phys. B 249 (1985) 42.
- 1457 [47] S. Biswas, E. Gabrielli and B. Mele, JHEP 1301 (2013) 088 [[arXiv:1211.0499 \[hep-ph\]](#)].
- 1459 [48] F. Demartin, B. Maier, F. Maltoni, K. Mawatari, and M. Zaro, “tWH associated  
 1460 production at the LHC”, European Physical Journal C, vol. 77, p. 34, (2017).  
 1461 [arXiv:1607.05862](#)
- 1462 [49] LHC Higgs Cross Section Working Group, “Handbook of LHC Higgs Cross  
 1463 Sections: 4.Deciphering the Nature of the Higgs Sector”, [arXiv:1610.07922](#).
- 1464 [50] J. Ellis, D. S. Hwang, K. Sakurai, and M. Takeuchi.“Disentangling Higgs-Top  
 1465 Couplings in Associated Production”, JHEP 1404 (2014) 004, [[arXiv:1312.5736](#)].
- 1466 [51] CMS Collaboration, V. Khachatryan et al., “Precise determination of the mass  
 1467 of the Higgs boson and tests of compatibility of its couplings with the standard  
 1468 model predictions using proton collisions at 7 and 8 TeV,” [arXiv:1412.8662](#).
- 1469 [52] ATLAS and CMS Collaborations, “Measurements of the Higgs boson produc-  
 1470 tion and decay rates and constraints on its couplings from a combined ATLAS

- 1471 and CMS analysis of the LHC pp collision data at  $sqrts = 7$  and 8 TeV,” (2016).  
 1472 CERN-EP-2016-100, ATLAS-HIGG-2015-07, CMS-HIG-15-002.
- 1473 [53] File:Cern-accelerator-complex.svg. Wikimedia Commons,  
 1474 the free media repository. Retrieved January, 2018 from  
 1475 <https://commons.wikimedia.org/wiki/File:Cern-accelerator-complex.svg>
- 1476 [54] J.L. Caron , “Layout of the LEP tunnel including future LHC infrastructures.”,  
 1477 (Nov, 1993). A C Collection. Legacy of AC. Pictures from 1992 to 2002. Re-  
 1478 trieval from <https://cds.cern.ch/record/841542>
- 1479 [55] M. Vretenar, “The radio-frequency quadrupole”. CERN Yellow Report CERN-  
 1480 2013-001, pp.207-223 DOI:10.5170/CERN-2013-001.207. arXiv:1303.6762
- 1481 [56] L.Evans. P. Bryant (editors). “LHC Machine”. JINST 3 S08001 (2008).
- 1482 [57] CERN Photographic Service.“Radio-frequency quadrupole, RFQ-1”, March  
 1483 1983, CERN-AC-8303511. Retrieved from <https://cds.cern.ch/record/615852>.
- 1484 [58] CERN Photographic Service “Animation of CERN’s accelerator net-  
 1485 work”, 14 October 2013. DOI: 10.17181/cds.1610170 Retrieved from  
 1486 <https://videos.cern.ch/record/1610170>
- 1487 [59] C.Sutton. “Particle accelerator”.Encyclopedia Britannica. July 17, 2013. Re-  
 1488 trieval from <https://www.britannica.com/technology/particle-accelerator>.
- 1489 [60] L.Guiraud. “Installation of LHC cavity in vacuum tank.”. July 27 2000. CERN-  
 1490 AC-0007016. Retrieved from <https://cds.cern.ch/record/41567>.
- 1491 [61] J.L. Caron, “Magnetic field induced by the LHC dipole’s superconducting coils”.  
 1492 March 1998. AC Collection. Legacy of AC. Pictures from 1992 to 2002. LHC-  
 1493 PHO-1998-325. Retrieved from <https://cds.cern.ch/record/841511>

- 1494 [62] AC Team. “Diagram of an LHC dipole magnet”. June 1999. CERN-DI-9906025  
1495 retrieved from <https://cds.cern.ch/record/40524>.
- 1496 [63] CMS Collaboration “Public CMS Luminosity Information”.  
1497 <https://twiki.cern.ch/twiki/bin/view/CMSPublic/LumiPublicResults#2016>  
1498 \_proton\_proton\_13\_TeV\_collis, last accessed 24.01.2018
- 1499 [64] J.L Caron. “LHC Layout” AC Collection. Legacy of AC. Pictures  
1500 from 1992 to 2002. September 1997, LHC-PHO-1997-060. Retrieved from  
1501 <https://cds.cern.ch/record/841573>.
- 1502 [65] CMS Collaboration. “The CMS experiment at the CERN LHC” JINST 3 S08004  
1503 (2008).
- 1504 [66] CMS Collaboration. “CMS detector drawings 2012” CMS-PHO-GEN-2012-002.  
1505 Retrieved from <http://cds.cern.ch/record/1433717>.
- 1506 [67] R. Breedon. “View through the CMS detector during the cooldown of the  
1507 solenoid on February 2006. CMS Collection”, February 2006, CMS-PHO-  
1508 OREACH-2005-004, Retrieved from <https://cds.cern.ch/record/930094>.
- 1509 [68] A. Dominguez et. al. “CMS Technical Design Report for the Pixel Detector  
1510 Upgrade”, CERN-LHCC-2012-016. CMS-TDR-11.
- 1511 [69] CMS Collaboration. “Description and performance of track and primary-vertex  
1512 reconstruction with the CMS tracker,” Journal of Instrumentation, vol. 9, no.  
1513 10, p. P10009,(2014).
- 1514 [70] CMS Collaboration and M. Brice. “Images of the CMS Tracker Inner  
1515 Barrel”, November 2008, CMS-PHO-TRACKER-2008-002. Retrieved from  
1516 <https://cds.cern.ch/record/1431467>.

- 1517 [71] M. Weber. “The CMS tracker”. 6th international conference on hyperons, charm  
1518 and beauty hadrons Chicago, June 28-July 3 2004.
- 1519 [72] CMS Collaboration. “Projected Performance of an Upgraded CMS Detector at  
1520 the LHC and HL-LHC: Contribution to the Snowmass Process”. Jul 26, 2013.  
1521 arXiv:1307.7135
- 1522 [73] L. Veillet. “End assembly of HB with EB rails and rotation in-  
1523 side SX”, January 2002. CMS-PHO-HCAL-2002-002. Retrieved from  
1524 <https://cds.cern.ch/record/42594>.
- 1525 [74] J. Puerta-Pelayo.“First DT+RPC chambers installation round in the  
1526 UX5 cavern.”. January 2007, CMS-PHO-OREACH-2007-001. Retrieved from  
1527 <https://cds.cern.ch/record/1019185>
- 1528 [75] X. Cid Vidal and R. Cid Manzano. “CMS Global Muon Trigger” web  
1529 site: Taking a closer look at LHC. Retrieved from [https://www.lhc-closer.es/taking\\_a\\_closer\\_look\\_at\\_lhc/0.lhc\\_trigger](https://www.lhc-closer.es/taking_a_closer_look_at_lhc/0.lhc_trigger)
- 1531 [76] WLCG Project Office, “Documents & Reference - Tiers - Structure,” (2014).  
1532 <http://wlcg.web.cern.ch/documents-reference> , last accessed on 30.01.2018.
- 1533 [77] CMS Collaboration, “Search for the associated production of a Higgs boson  
1534 with a single top quark in proton-proton collisions at  $\sqrt{s} = 8$  TeV”, JHEP 06  
1535 (2016) 177,doi:10.1007/JHEP06(2016)177, arXiv:1509.08159.
- 1536 [78] B. Stieger, C. Jorda Lope et al., “Search for Associated Production of a Single  
1537 Top Quark and a Higgs Boson in Leptonic Channels”, CMS Analysis Note CMS  
1538 AN-14-140, 2014.

- 1539 [79] M. Peruzzi, C. Mueller, B. Stieger et al., “Search for ttH in multilepton final  
1540 states at  $\sqrt{s} = 13$  TeV”, CMS Analysis Note CMS AN-16-211, 2016.
- 1541 [80] CMS Collaboration, “Search for H to bbar in association with a single top quark  
1542 as a test of Higgs boson couplings at  $\sqrt{s} = 13$  TeV”, CMS Physics Analysis  
1543 Summary CMS-PAS-HIG-16-019, 2016.
- 1544 [81] B. Maier, “SingleTopHiggProduction13TeV”, February, 2016.  
1545 <https://twiki.cern.ch/twiki/bin/viewauth/CMS/SingleTopHiggsGeneration13TeV>.
- 1546 [82] M. Peruzzi, F. Romeo, B. Stieger et al., “Search for ttH in multilepton final1  
1547 states at  $\sqrt{s} = 13$  TeV”, CMS Analysis Note CMS AN-17-029, 2017.
- 1548 [83] B. WG, “BtagRecommendation80XReReco”, February, 2017.  
1549 <https://twiki.cern.ch/twiki/bin/view/CMS/BtagRecommendation80XReReco>.